Combustion and Flame 269 (2024) 113697

Contents lists available at ScienceDirect

Combustion and Flame

journal homepage: www.sciencedirect.com/journal/combustion-and-flame

# Kinetic modeling of carbonaceous particle morphology, polydispersity and nanostructure through the discrete sectional approach

Andrea Nobili, Niccolò Fanari, Timoteo Dinelli, Edoardo Cipriano, Alberto Cuoci, Matteo Pelucchi, Alessio Frassoldati, Tiziano Faravelli *

*CRECK Modeling Lab, Department of Chemistry, Materials and Chemical Engineering "G. Natta", Politecnico di Milano, P.zza Leonardo da Vinci 32, Milano 20133, Italy*

ARTICLE INFO

*Keywords:*
Carbonaceous nanoparticles
Morphology
Nanostructure
Kinetic model

ABSTRACT

Carbon nanoparticle (CNP) formation from hydrocarbons combustion is of high interest not only for the study of pollutant (soot) emissions, but, above all, in the area of advanced materials. CNP optical and electronical properties, relevant for practical applications, significantly change with their size, morphology, and nanostructure. This work extends a detailed soot kinetic model, based on the discrete sectional approach, to explicitly incorporate the description of CNP polydispersity, maintaining the CHEMKIN-like format. The model considers various nanosized primary particles, generated from liquid-like counterparts through the carbonization process, which successively grow or aggregate forming fractal structures. The model is validated against experimental measurements from the literature including CNP volume fraction, several morphological characteristics, number density and particle H/C ratio. Data are taken from 19 laminar flames, in different configurations (counterflow diffusion flames, premixed flat flames established on the McKenna-type burner and burner-stabilized stagnation flames) and over a wide range of operating conditions (P=1–10 atm, $T_{max}$=1556-2264 K). The model captures the measured trends of all the analyzed CNP properties as a function of equivalence ratio, residence time and fuel type in premixed flames, and pressure and strain rate in counterflow flames. Model deviations from the experiments are discussed, also in comparison with other state-of-the-art soot models based on different approaches. Sensitivity analyses are performed on carbonization, coalescence, and aggregation rates, which have the largest impact on CNP morphology and are characterized by larger uncertainty compared to elementary chemical pathways.

## 1. Introduction

Recent scientific research is driving a paradigm shift on carbonaceous nanoparticles (CNPs) produced from hydrocarbon combustion, looking more and more often at them as attractive materials for new practical applications rather than as harmful pollutants [1,2].

The strong variation of the physical and chemical characteristics of such particles as their size and nanostructure evolve in laminar flames was highlighted in several studies. CNPs formed in flames exhibit quantum dot behavior [3]. The size-specific electronic and optical properties of CNPs were measured [3–5] and modeled [6], demonstrating the variation of ionization energies and optical band gaps with particle diameter. An experimental setup for flame synthesis and sampling of CNPs was recently proposed easing the separation of fluorescent nanocarbons of less than 20 nm in size [7]. The different absorption and emission properties, such as particle quantum yield and optical band gap, of such particles were studied by varying the equivalence ratio and the fuel composition in ethylene and ethylene/benzene premixed flames [8]. It was shown that CNP properties can be tuned by changing particle diameter and optical band gap at fixed crystallinity and residence time [8]. As the particle diameter increases, the nanostructure of CNPs also changes [9,10]. The amount of elemental carbon (which absorbs visible light) in CNPs produced in a laminar premixed ethylene flame increases moving from 2-4 nm to 4-24 nm particles, while the content of organic carbon (which does not absorb visible light) exhibits an opposite trend [9]. This change in the nanostructure as the diameter increases is reflected in a higher graphitization level [11] and a variation of the particle optical properties, such as a decrease in the mass absorption coefficient evaluated through thermo-optical analysis [9]. It is worth noting that all the optical and electronic properties of these carbonaceous nanoparticles are not related to any surface functionalization, but

* Corresponding author.
*E-mail address:* tiziano.faravelli@polimi.it (T. Faravelli).

https://doi.org/10.1016/j.combustflame.2024.113697
Received 25 March 2024; Received in revised form 23 August 2024; Accepted 23 August 2024
Available online 30 August 2024

**Nomenclature**

| | |
|---|---|
| $BIN_{i,j}$ | lumped pseudo-species of the i-th mass section and j-th H/C level |
| $BIN_{i,j}$-L | BINs indicating liquid-like particles |
| $BIN_{i,j}$-PP | BINs indicating primary particles |
| $BIN_{i,j}$-AG-k | BINs indicating aggregates of type k |
| $f_v$ | volume fraction |
| $D_{pp,i}$ | primary particle diameter of each BIN |
| $D_{pp}$ | average primary particle diameter |
| $D_{63}$ | average particle size |
| $D_f$ | fractal dimension |
| $N_i$ | number density of each BIN |
| $N_{pp,i}$ | number density of each primary particle |
| $n_{pp,i}$ | number of primary particles within each aggregate |
| $w_i$ | mass fraction of each BIN |
| $m_i$ | mass of each BIN |
| We | Weber number |
| $d_p$ | diameter of liquid-like nanoparticles |
| $v_r$ | relative velocity |
| $K_G$ | global strain rate |
| $Z_{st}$ | stoichiometric mixture fraction |
| $z_{stg,p}$ | particle stagnation plane |
| $z_{Tmax}$ | flame front |
| $T_{max}$ | maximum flame temperature |
| P | pressure |
| $v_0$ | inlet cold gas velocity |

*Greek symbols*

| | |
|---|---|
| $\rho$ | particle density |
| $\rho_{mix}$ | gas mixture density |
| $\sigma_s$ | surface tension |
| $\phi$ | equivalence ratio |

*Acronyms*

| | |
|---|---|
| BSS | burner-stabilized stagnation |
| PAH | polycyclic aromatic hydrocarbon |
| CNP | carbonaceous nanoparticle |
| PSD | particle size distribution |
| PPSD | primary particle size distribution |

merely to their size and nanostructure.

Regarding CNP morphology, it is known that polydisperse aggregates are formed by primary particles of different sizes [12–14]. Great efforts have been made to develop kinetic models that can describe this polydispersity in flames [12,15–17]. Thomson and coworkers [16,18–22] developed an advanced sectional model, based on the solution of transport equations for the number density of aggregates and primary particles, as well as the number density of H-atoms of each section considered. Bodor et al. [23] also proposed a post processing technique to predict the primary particle size of premixed and coflow ethylene sooting flames based on a discrete sectional model. Kraft and coworkers [14] proposed a detailed population balance model (PBM) [14,24–28], which describes the evolution of carbonaceous particles by solving the Smoluchowski equation [29] with additional terms that account for many physico-chemical pathways underlying CNP dynamics in flames. Through this stochastic approach, it was also possible to track the structure of individual PAHs within the primary particles, which constitute carbonaceous aggregates [25,26]. However, thermophoretic effect and particle diffusivity cannot be accounted for. Kelesidis et al. [12,30] developed a discrete element model (DEM) that solves ballistic trajectories of an initial number of particles with assigned diameter and number density. This model considers key processes like agglomeration and surface growth to predict the evolution of particle size and aggregate characteristics (e.g., fractal dimension, effective density, number of primary particles per aggregate). The DEM model was also used to derive scaling laws to optimize optical diagnostics for CNPs. All these models were successfully applied in both one and two-dimensional flame simulations to predict several structural soot measurements [16,31,32].

This work presents the first discrete sectional model fully written in CHEMKIN-like format [33] and coupled with a detailed gas-phase chemistry that can predict CNP morphology in terms of average particle size ($D_{63}$) profiles, primary particle diameter ($D_{pp}$) profiles and particle size distributions together with volume fraction ($f_v$), number density and H/C ratio along one-dimensional laminar flames. The proposed model has several advantages over existing models developed for a detailed description of carbonaceous particle morphology. One of the main advantages is that neither the solution of many additional equations other than those for mass, energy, momentum, and species, nor post-processing steps of numerical results obtained through simplified methods are required. Particle thermophoresis, diffusivity and radiation are considered. Moreover, the proposed model allows to account for the different reactivity of aggregates that share equivalent mass but possess different surface areas, i.e., reactive sites, due to the possible presence of primary particles of different sizes. On the other hand, the computational cost associated to numerical simulations performed with the present model is higher than that of models based on the method of moments [34,35]. Conversely, the associated computational cost is lower compared to models based on stochastic approaches [34], which however can provide an even more detailed description of CNP morphology, e.g., by considering a possible overlapping of primary particles within fractal structures [31].

The paper is structured as follows: Section 2 provides the description of the polydisperse kinetic model. Model validation against CNP data of laminar premixed and counterflow flames available in the literature is reported in Sections 3.1-3.3. In Section 3.4 a brute force sensitivity analysis is performed on the key reaction classes controlling the evolution of CNP morphology, and the results are discussed.

## 2. Materials and methods

### 2.1. CRECK polydisperse sectional model

The main features of the discrete sectional model developed by the CRECK modeling group were described in previous works [36–39] and are maintained in the proposed polydisperse model. Large PAHs and CNPs are discretized into 25 sections of lumped pseudo species, called BINs, from 20 to over $10^8$ C-atoms, with a spacing factor of two between the number of C-atoms of adjacent sections. To accurately describe maturation processes, three different H/C ratios (A, B, C) are considered for sections from BIN1 to BIN14. For BIN15-19 and for BIN20-25 two and one H/C ratios are considered, respectively, as the hydrogenation level of large carbonaceous particles tends to a constant value [40]. The H/C ratio assigned to each BIN is specified in Table S2 of the Supplementary Material (SM). BIN1-4 represent large PAHs, while BIN5, with 320 C-atoms and a diameter of ~2 nm, is selected as the smallest particle. Based on a recent theoretical study on large PAHs [41], aromatic species with >100 C-atoms (from BIN4) are modeled as persistent radicals, denoted with letter "J".

In this work, the assumption of primary particles (BIN12) with a single fixed size, i.e., ~10 nm, adopted in previous versions of the model [36–39], is removed to account for polydispersity. This enables an improved description of the morphology and in turn of the surface reactivity of carbonaceous particles.

Fig. 1 shows that once the first liquid-like particles form through inception of gas-phase large PAHs, they can coalesce or grow towards larger BIN-L (vertical arrows, "C&G") or undergo carbonization towards primary particles BIN-PP (horizontal arrows, "LtoS"). Liquid-like and primary particle size ranges from $D_{pp} = 2$ nm (BIN5J-L and BIN5J-PP) to $D_{pp} = 97$ nm (BIN22J-L and BIN22J-PP). This range guarantees covering the evolution of the average primary particle diameters in laminar flames up to 10 atm [42,43].

Indeed, it was experimentally observed that incipient particles are liquid-like amorphous carbonaceous materials [40,45,46]. Then, an interplay of physicochemical phenomena governs the transition from liquid-like to solid particles. As discussed in [47], this transition is driven by the carbonization and graphitization processes, which include both particle dehydrogenation, functional-group elimination, and molecular rearrangement. The modification of the crystallite-layer planes of a carbonaceous material towards graphite nanostructure [47] leads to more carbonized and graphitic structures as the particle residence time in the high-temperature flame region increases [44,48].

Dobbins [49] proposed a first-order Arrhenius rate constant for the conversion of CNP precursor particles to carbonaceous species in diffusion flames of eight different hydrocarbon fuels, from lightly sooting methane to highly sooting benzene. An activation energy of 27 kcal/mol was proposed in [49], indicating that the formation of primary particles from their liquid-like counterparts is fostered as the temperature increases. This rate, used in the model proposed by Kholghy et al. [44] to describe the reorganization of the PAH clusters within particles moving from nascent to mature CNPs [50], is also here considered. However, in the present model the reference carbonization kinetics is scaled based on the H/C ratio and on the diameter of each BIN-L, by assuming that more graphitic and larger liquid-like particles carbonize faster [10,50]. The adopted scaling factor (see Table 1) is chosen to better capture the average primary particle diameter profiles in the laminar flames analyzed in Section 3.1.

Primary particles can then form larger BIN-PP through coagulation and growth (vertical arrows in Fig. 1) or Aggregate ("A") into fractals (diagonal arrows in Fig. 1). The combination of primary particles of different size within the same aggregate would result in an enormous number of BINs. So, in order to limit as much as possible the total number of species in the proposed model, each primary particle is assumed to aggregate forming discrete, lumped monodisperse entities, similarly to [51], with a fractal dimension $D_f = 1.8$ [52]. Specifically, 18 different aggregate types (BIN-AG-k in Fig. 1) are considered, from $BIN_i$-AG-I (with i from 6 to 25) constituted by BIN5J-PP to $BIN_i$-AG-XVIII constituted by BIN22J-PP (with i from 23 to 25). If polydisperse aggregates are produced, i.e., by the combination of primary particles with different size, they are split, with the right proportion, among monodisperse BIN-AG available in the kinetic model and constituted by one of the two BIN-PP reactants, as detailed in the following of this section.

Different monodisperse aggregates (e.g., BIN-AG-I, BIN-AG-II) with equal mass are considered in the model (Fig. 1). As an example, BIN7AJ-AG-I and BIN7AJ-AG-II represent two aggregates with equal number of C-atoms and H/C level (BIN7AJ) constituted by four BIN5AJ-PP and two BIN6AJ-PP primary particles, respectively.

The reactions between the different type of CNPs presented in Fig. 1 are balanced under the following assumptions:

**Table 1**

Reaction classes and reference Arrhenius-like rate parameters, $k = AT^n\exp\left(-\frac{E}{RT}\right)$, adopted for carbonization, coalescence and aggregation. $\gamma$ is the collision efficiency adopted from [37]. Units are cm, mol, kcal, K. $V_{big}$ and $V_{small}$ represent the volume of the larger and smaller colliding BIN, respectively, during coalescence.

| Reaction classes | A | n | E | Ref. |
|---|---|---|---|---|
| *1. Carbonization* | | | | |
| RC1: BIN-L → BIN-PP | $1.8 \times 10^6 \frac{C/H}{C/H_{ref}} \frac{D}{D_{ref}}$ | 0 | 27 | [49] |
| *2. Coalescence* | | | | |
| RC2: BIN-L + BIN-L/PP/AG → products | $4.0 \times 10^{13} \frac{V_{big}}{V_{small}}$ | 0.5 | 0 | this work |
| *3. Aggregation* | | | | |
| RC4: BIN-PP/AG + BIN-PP/AG → products | $4.0 \times 10^{13} nC^{1/6} \gamma$ | 0.5 | 0 | [37,54] |

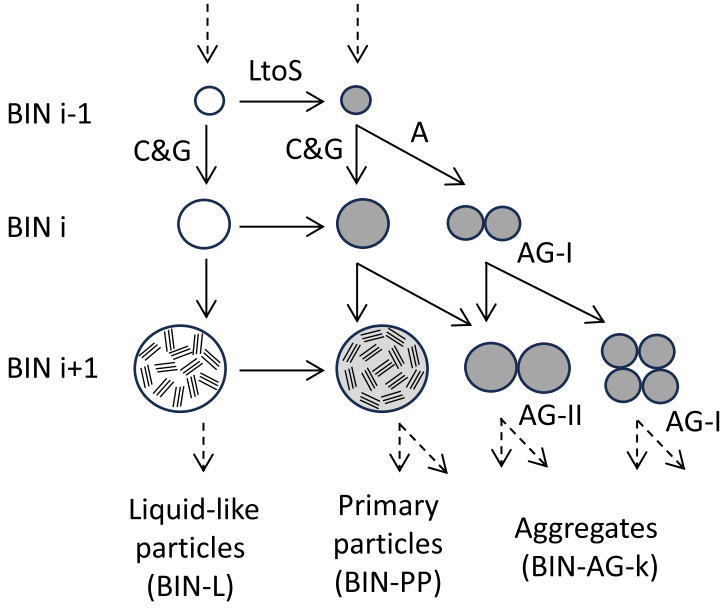


**Fig. 1.** Schematization of the polydisperse CRECK model. The arrows represent different reaction classes: carbonization, i.e., the transition from liquid to solid particles ("LtoS", adapted from [44]), coalescence and surface growth ("C&G"), and aggregation ("A"). Inception, dehydrogenation, and oxidation reaction classes, not shown in this figure, are also included in the model. 18 liquid-like and primary particle sizes are considered, from BIN5 to BIN22, with 18 different aggregate types (BIN-AG-k, with k from I to XVIII, as detailed in Table S2 of the SM).

- Stoichiometric coefficients of the BIN products are calculated from the H- and C-atom balances, as explained in [53]. For example:

R1) $C_2H_2$ + BIN5BJ-PP => 0.009914 BIN5AJ-PP + 0.983836 BIN5BJ-PP + 0.000045 BIN6AJ-PP + 0.006205 BIN6BJ-PP

In the example, the effective product resulting from acetylene addition to BIN5BJ-PP is split firstly between adjacent BIN sections through the lever rule on C-atoms (BIN5 and BIN6) and then between adjacent hydrogenation levels through the lever rule on H/C ratios (A and B) [53], as sketched in Fig. 2a.

- For BIN-L coalescence on BIN-PP, a single larger spherical BIN-PP is produced thus maintaining the number of solid primary particles in the reactive system. For example:

R2) BIN5AJ-L+BIN7BJ-PP => 0.167560 BIN7AJ-PP + 0.576440 BIN7BJ-PP + 0.060831 BIN8AJ-PP + 0.195169 BIN8BJ-PP
Same BIN products of R2 are obtained from BIN7BJ-L + BIN5AJ-PP.

- For BIN-L coalescence on BIN-AG, larger fractals constituted by primary particles of the same $D_{pp}$ size of the reactant BIN-AG are produced. For example:

R3) BIN5AJ-L + BIN7BJ-AG-I => 0.167560 BIN7AJ-AG-I + 0.576440 BIN7BJ-AG-I + 0.060831 BIN8AJ-AG-I + 0.195169 BIN8BJ-AG-I
For reactions R2 and R3, the effective product splits among the BINs available in the kinetic model through the same approach depicted in Fig. 2a for R1.

- For BIN-PP/AGG + BIN-PP/AGG reactions, i.e., when the two reactants are constituted by primary particles of different $D_{pp}$, stoichiometric coefficients are firstly calculated from the H- and C-atom balances adopted for all the other reactions of the BINs, as explained in [53]. Then, BIN products are further split in order to balance the number and the size of reactant primary particles. For example:

R4) BIN6AJ-PP + BIN10BJ-PP => 0.066662 BIN10AJ-PP + 0.810974 BIN10BJ + 0.004875 BIN11AJ-AG-VI + 0.055134 BIN11BJ-AG-VI + 0.004433 BIN10AJ-AG-II + 0.053931 BIN10BJ-AG-II + 0.000324 BIN11AJ-AG-II + 0.003667 BIN11BJ-AG-II
R5) BIN6AJ-PP + BIN10BJ-AG-I => 0.066662 BIN10AJ-AG-I + 0.810974 BIN10BJ-AG-I + 0.0048751 BIN11AJ-AG-I + 0.055134 BIN11BJ-AG-I + 0.004433 BIN10AJ-AG-II + 0.053931 BIN10BJ-AG-II + 0.000324 BIN11AJ-AG-II + 0.003667 BIN11BJ-AG-II
R6) BIN6AJ-AG-I + BIN10BJ-AG-II => 0.004433 BIN10AJ-AG-I + 0.053931 BIN10BJ-AG-I + 0.000324 BIN11AJ-AG-I + 0.003667 BIN11BJ-AG-I + 0.066662 BIN10AJ-AG-II + 0.810974 BIN10BJ-AG-II + 0.004875 BIN11AJ-AG-II + 0.055134 BIN11BJ-AG-II

In these examples, one mole of BINs is always produced, i.e., the sum of the stoichiometric coefficients of the products is equal to 1, and lever rules on C-atoms and on H/C ratios from adjacent BIN sections are applied as in R1. A further split is then applied to balance the number of primary particles (PP) in the BIN reactants and products: 1 BIN6-PP and 1 BIN10-PP in R4, 1 BIN6-PP and 32 BIN5-PP (within BIN10-AG-I) in R4, 2 BIN5-PP (within BIN6-AG-I) and 16 BIN6-PP (within BIN10-AG-II) in R6.

Fig. 2b exemplifies the multiple splits performed for reaction R4 on the effective product, represented by a polydisperse aggregate, among the BIN-PP and monodisperse BIN-AG available in the kinetic model. As in the case of reactions not involving the formation of polydisperse aggregates (Fig. 2a), the lever rules on the number of C-atoms (nC-split) and H/C ratio (H/C-split) split the effective product, i.e., the black aggregate in Fig. 2b, into the adjacent smaller (BIN10) and larger (BIN11) discrete species considered in the model (white aggregates). These latter species must be further split (PP-split in Fig. 2b) to be converted from polydisperse entities to monodisperse aggregates (or spherical particles), among those included in the model, in order to conserve the number and the size of primary particles between BIN reactants and products. Specifically, in reaction R4 the two reactants are BIN6AJ-PP, i.e., the second primary particle considered in the model (after BIN5-PP) which leads to $BIN_i$-AG-II species (see Fig. 1), with i>6, and BIN10BJ-PP, i.e., the sixth primary particle considered which leads to $BIN_i$-AG-VI species, with i>10. The resulting final BIN products (grey particles and aggregates in Fig. 2b) are constituted either by a high number of the smaller reactant BIN6-PP (BIN10AJ-AG-II, BIN10BJ-AG-II, BIN11AJ-AG-II, BIN11BJ-AG-II) or by a low number of the larger reactant BIN10-PP (BIN10AJ-PP, BIN10BJ-PP, BIN11AJ-AG-VI, BIN11BJ-AG-VI), with the proportion given by the stoichiometric coefficients in R4, that allows to reconstruct the effective polydisperse product. The same logic applies for reactions R5 and R6.

Table 1 reports the reference rate parameters of coalescence and aggregation reactions, along with those for the carbonization pathway introduced in the present model. The reference rate parameters for aggregation of solid particles and aggregates are adapted from previous versions of the model [37–39]. In particular, the collision efficiency ($\gamma$)

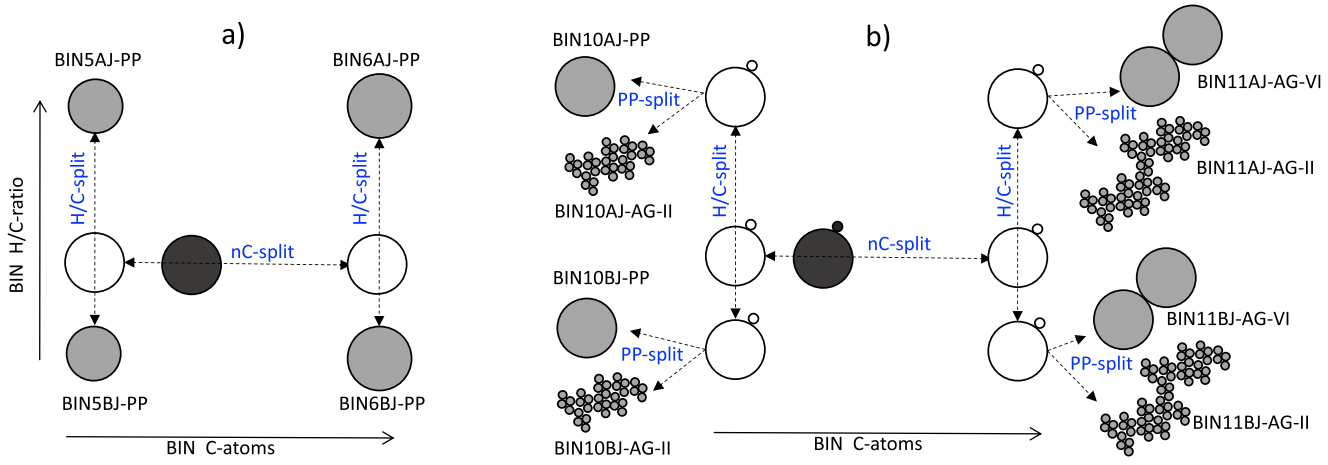


**Fig. 2.** Schematization of the effective product (black circles) splitting among the BINs available in the model (grey circles), carried out by applying the lever rule [53] on the number of C-atoms and H/C ratio, for a) reaction R1 and, additionally, on the number of primary particles for b) reaction R4.

proposed by Sirignano et al. [54] and refined by Pejpichestakul et al. [37] is considered to account for the temperature, particle H/C ratio and size dependency of aggregation reactions. The reference pre-exponential factor (A) is also scaled based on the total number of C-atoms (nC) of the BIN reactants [37,54]. A=4.0 × $10^{13}$ $cm^3$/mol/s, which lies in between the reference pre-exponential factor used by Sirignano et al. [54] (0.8 × $10^{13}$ $cm^3$/mol/s), Pejpichestakul et al. [37] (1.6 × $10^{13}$ $cm^3$/mol/s) and Saggese et al. (1.5 × $10^{14}$ $cm^3$/mol/s), is considered to obtain a better agreement with literature experiments.

For coagulation, which involves at least one liquid-like particle (BIN-L), different rates are instead considered. In particular, a unitary collision efficiency ($\gamma = 1$) is assumed, as in [55]. In this regard, it is possible to estimate the Weber number, which is a non-dimensional number that characterizes droplet collision regimes (e.g., coalescence, bouncing, stretching, break-up) for different species at both the micro- and the nano-scale [56–58], through Equation 1:

$$We = \frac{\rho d_p v_r^2}{\sigma_s} \tag{1}$$

Independently of the possible ranges of density ($\rho$, in the order of $10^2$-$10^3$ kg/$m^3$ [59]), surface tension ($\sigma_s$, $10^{-2}$-$10^{-1}$ N/$m^3$ for heavy hydrocarbons in air [60]) and relative velocity ($v_r$, $10^{-2}$-$10^{-1}$ m/s) that CNPs may experience in laminar flames, We << 1 is obtained, i.e., complete coalescence regime [56], due to the nano-size diameter ($d_p$, $10^{-9}$-$10^{-7}$ m) of carbonaceous particles.

The numerical study by Hawa and Zachariah [61] is also considered to assess coalescence rates. The authors investigated coalescence mechanisms of pairs of unequal sized silicon nanoparticles, thus a non-carbonaceous material, using molecular dynamics (MD) simulations under constant temperature conditions. As in the case of carbonaceous particles [62], the driving force for coalescence of silicon nanoparticles is the minimization of the surface free energy [61]. Fig. 3 shows the calculated coalescence time of unequal sized liquid nanoparticles, normalized by the one for two equal sized particles, as a function of the volume ratio of the colliding entities at 1500 K. Importantly, it can be observed that MD simulation results by Hawa and Zachariah [61] well agree with the model developed by Koch and Friedlander (KF) [63], who generalized the Smoluchowski equation [64] to incorporate the coalescence rate into the aerosol dynamics and applied their model to fine particle formation in combustion processes under non-isothermal conditions.

Based on these studies, coagulation rates are here scaled with respect to the spherical-equivalent volume ratio of the colliding entities, as reported in Table 1. This assumption allows to drastically improve the predictions of particle size distribution in laminar premixed flames compared to previous versions of the model, as it will be discussed in Section 3.2.

Reaction classes for inception, surface growth, dehydrogenation and oxidation with their reference rate parameters are taken from previous versions of the CRECK model [37–39] and are reported in Table S1 of the SM.

To highlight the variation of surface reactivity with the particle/aggregate morphology, Fig. 4 shows the rate constant for acetylene ($C_2H_2$) addition to pseudo species having equivalent mass (BIN12AJ) but different surface area. By comparing acetylene addition on an aggregate made of larger (i.e., 2 BIN-11AJ-PP in BIN12AJ-AG-VII) and smaller primary particles (i.e., 128 BIN5AJ-PP in BIN12AJ-AG-I), the rate constant increases by a factor of ~5. Such remarkable variation in the surface kinetics can be described only through a polydisperse model. Fig. 4 also shows the reference gas-phase kinetics adopted from the gas-phase CRECK model. It is more than one order of magnitude lower with respect to analogous carbonaceous particle/aggregate reactions, for which the pre-exponential factor is scaled as a function of the surface area, as proposed by Saggese et al. [36].

### 2.2. Numerical simulations

The overall model, coupled with detailed gas-phase chemistry up to 5-ring aromatic species ($C_{18}H_{10}$ and $C_{18}H_{14}$) [65,66], comprises 709 species and 130449 reactions and it is available in CHEMKIN format as SM. Numerical simulations of one-dimensional laminar premixed flames, with (BSSF) and without a water-cooled stagnation plate, and counterflow diffusion flames are carried out with the OpenSMOKE++ framework [67] using the 1-D laminar flame solver, including the mixture-average diffusion coefficient, the Soret effect, gas and soot radiation [68], and particle thermophoresis in the species transport equations.

With respect to CNP polydispersity, the number density of each primary particle ($N_{pp,i}$) is obtained from the mass fractions of the primary particles and aggregates (Equation 2). Then, from $N_{pp,i}$, both the average primary particle diameter (Equation 3) and the primary particle size distribution can be calculated along the temporal/spatial coordinate of any ideal reactor or laminar flame:

$$N_{pp,i} = N_i \cdot n_{pp,i} = \left(\frac{\rho_{mix}}{m_i} w_i\right) \cdot n_{pp,i} \tag{2}$$

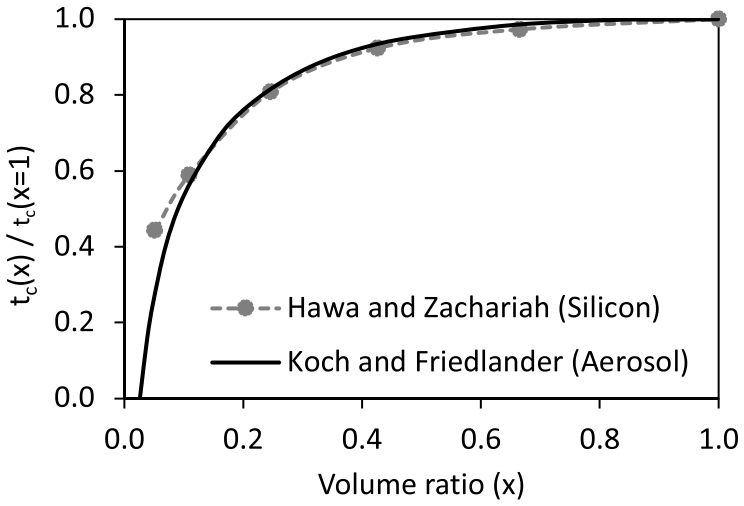


**Fig. 3.** Normalized coalescence times of liquid-like silicon [61] and aerosol [63] nanoparticles as a function of initial particle volume ratio at 1500 K. Adapted from [61].

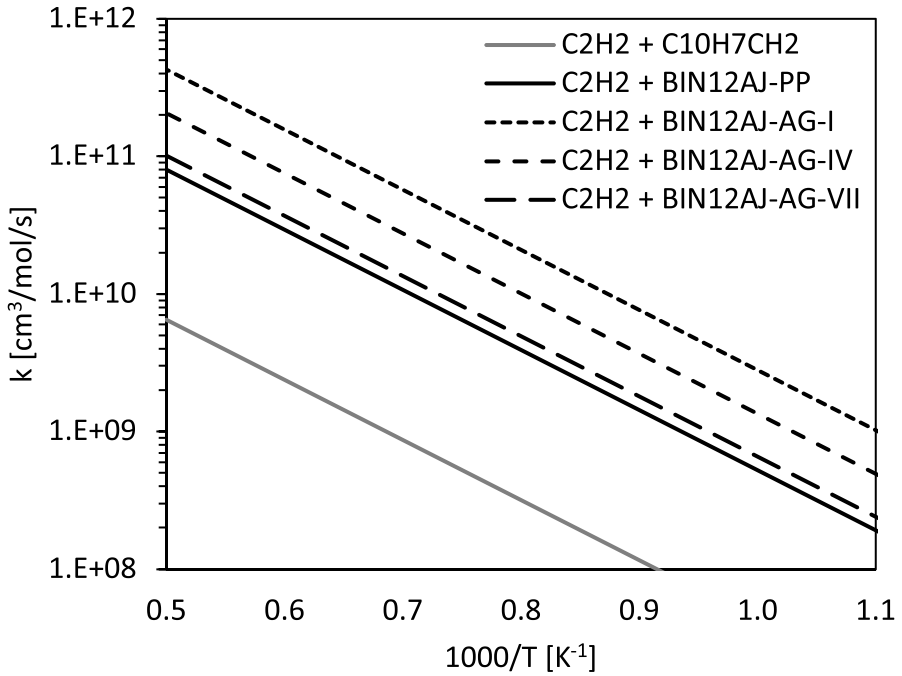


**Fig. 4.** Rate constant of acetylene ($C_2H_2$) on primary particles and BIN12AJ monodisperse aggregates constituted by different-size primary particles. Comparison with the reference kinetics from the gas-phase mechanism, i.e., $C_2H_2$+$C_{10}H_7CH_2$ (methyl-naphthyl resonance-stabilized radical), is also reported.

$$D_{pp} = \frac{\sum_{i=1}^{N} D_{pp,i} \cdot N_{pp,i}}{\sum_{i=1}^{N} N_{pp,i}} \quad (3)$$

where $m_i$, $w_i$ and $N_i$ represent the mass, the mass fraction and the number density of each *i*-th primary particle or aggregate included in the model, respectively. $\rho_{mix}$ is the density of the gas-phase mixture. $D_{pp,i}$ and $n_{pp,i}$ are the diameter (from ~2 nm for BIN5 to ~190 nm for BIN25 [38]) and the number of primary particles (>1 for aggregates), respectively, assigned to each BIN (see Table S2 in the SM).

## 3. Results and discussions

Model validation is performed by comparison with data from 19 laminar flames, whose operating conditions are summarized in Table 2. The selected flames include three different configurations: premixed flat flames established on the McKenna-type burner, premixed burner-stabilized stagnation flames and counterflow diffusion flames. Most of these flames are selected as target flames in the ISF database [69] and provide several morphological data of the collected carbonaceous particles along with volume fraction measurements. The investigated diffusion flames belong to the so-called soot formation (SF) counterflow flames and are characterized by a negligible role of particle oxidation [42,43,70]. The experiments and model simulations for the flames in Table 2 are also available in the SciExpeM database [71] (see Table S3 of the SM).

### 3.1. Average primary particle diameter

The series of premixed ethylene flames experimentally studied by Xu et al. [72] and the series of counterflow diffusion ethylene flames by Amin et al. [42] are firstly selected to assess the model performances against literature data. Indeed, these two series of laminar flames include measurements of average primary particle diameter ($D_{pp}$) together with volume fraction profiles ($f_v$), at different equivalence ratios ($\phi$ = 2.34-2.94) and pressures (P = 2-5 atm) in the premixed and in the counterflow configuration, respectively. The operating conditions of the selected premixed (F1-F3) and counterflow flames (F9-F12) are summarized in Table 2.

**Table 2**
Laminar flames investigated.

| #Flame | $T_{max}$ [K] | P [atm] | $\phi$ | [a]$v_0$ [cm/s] | L [mm] | Targets | Ref. |
|---|---|---|---|---|---|---|---|
| Premixed | | | | | | | |
| F1 | 1644 | 1 | 2.34 | 6.80 | 30 | $f_v$, $D_{pp}$ | [72] |
| F2 | 1600 | 1 | 2.64 | 6.80 | 30 | $f_v$, $D_{pp}$ | [72] |
| F3 | 1556 | 1 | 2.94 | 6.80 | 30 | $f_v$, $D_{pp}$ | [72] |
| F4 | 1700 | 1 | 2.40 | 4.00 | 14 | $f_v$, H/C | [40] |
| [b]F5 | 1770 | 1 | 2.40 | 5.00 | 16 | $f_v$, H/C | [40] |
| BSS | | | | | | | |
| F6 | 1783 | 1 | 2.06 | 8.00 | 5 | PSD | [73] |
| F7 | 1817 | 1 | 2.06 | 8.00 | 7 | PSD | [73] |
| F8 | 1832 | 1 | 2.06 | 8.00 | 10 | PSD | [73] |
| Counterflow | | | [c]$Z_{st}$ | [d]$K_G$ [1/s] | | | |
| F9 | 1983 | 2 | 0.170 | 30 | 8.2 | $f_v$, $D_{pp}$ | [42] |
| F10 | 2016 | 3 | 0.170 | 30 | 8.2 | $f_v$, $D_{pp}$ | [42] |
| F11 | 2037 | 4 | 0.170 | 30 | 8.2 | $f_v$, $D_{pp}$ | [42] |
| F12 | 2052 | 5 | 0.170 | 30 | 8.2 | $f_v$, $D_{pp}$ | [42] |
| F13 | 2264 | 1 | 0.068 | 38 | 8 | $f_v$, $D_{63}$ | [70] |
| F14 | 2253 | 1 | 0.068 | 50 | 8 | $f_v$, $D_{63}$ | [70] |
| F15 | 2245 | 1 | 0.068 | 63 | 8 | $f_v$, $D_{63}$ | [70] |
| F16 | 2239 | 1 | 0.068 | 75 | 8 | $f_v$, $D_{63}$ | [70] |
| F17 | 1936 | 5 | 0.253 | 30 | 8 | PPSD | [43] |
| F18 | 1954 | 7 | 0.253 | 30 | 8 | PPSD | [43] |
| F19 | 1967 | 10 | 0.253 | 30 | 8 | PPSD | [43] |

[a] Cold gas inlet velocity
[b] F5 is a methane flame. All the other flames are fueled with ethylene.
[c] Stoichiometric mixture fraction and
[d] global strain rate defined in [74].

Fig. 5 shows the comparisons between measured and simulated $f_v$ and $D_{pp}$ profiles of the two series of laminar ethylene flames.

In the series of premixed flames, the model captures the increase of both volume fraction (Fig. 5a) and average primary particle diameter (Fig. 5b) as the equivalence ratio increases. A good quantitative agreement between measurements and simulations is obtained for both

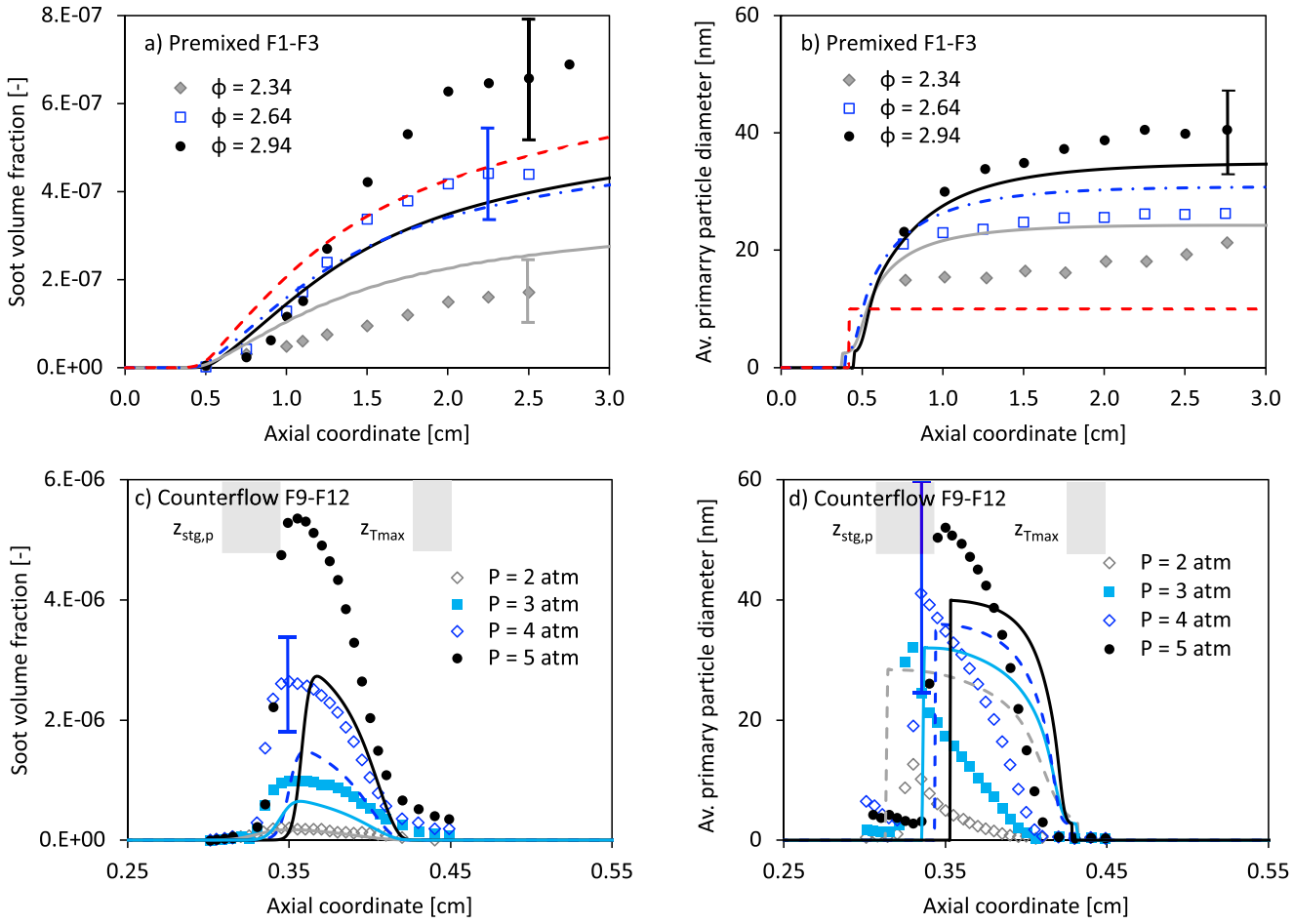


**Fig. 5.** (a, c) Soot volume fraction ($f_v$) and (b, d) average primary particle diameter ($D_{pp}$) profiles in laminar ethylene premixed (P=1 atm, $v_0$=6.8 cm/s, ϕ =2.34-2.94 [72], F1-F3 in Table 2) and counterflow flames (P=2-5 atm, $X_f$ = 0.3, $Z_{st}$=0.170, $K_G$=30 $s^{-1}$ [42], F9-F12 in Table 2). Symbols: experiments; lines: model simulations. Red dashed lines in a) and b) are the results of the previous version [37] of the present model at ϕ =2.64.

carbonaceous particle properties at $\phi$ = 2.34 and 2.64, while larger deviations occur at $\phi$ = 2.94, where $f_v$ is underestimated by a factor of 1.8 and results very similar to the $f_v$ calculated at $\phi$ = 2.64, differently from the experimental values. However, it can be noted that the confidential intervals of measured $f_v$ profiles at $\phi$ = 2.64 and 2.94 result partially overlapped by considering the experimental uncertainty of ~30% reported for the investigated data [72]. On the other hand, the evolution of $D_{pp}$ profiles along the axial coordinate of the flame at different equivalence ratios is well reproduced, with maximum deviations by a factor of ~1.2 at $\phi$ = 2.94. Importantly, Fig. 5b shows the improved predictive capability of the proposed model, which accounts for CNP polydispersity, with respect to its previous version [37], which instead assumes monodisperse aggregates constituted by fixed size primary particles ($D_{pp}$=10 nm) and cannot describe the evolution of the $D_{pp}$ profile, independently of equivalence ratio and other flame conditions. Fig. 5a also shows $f_v$ predicted by the current model and by its previous version [37] at $\phi$ = 2.64. The quantitative discrepancy (< 30%) in the respective $f_v$ profiles is primarily due to the underlying different particle surface chemistry, higher in the monodisperse model due to the assumption of fixed primary particle size. In fact, the $D_{pp}$ profile results smaller than that obtained with the present model along the flame from >0.6 cm above the burner (Fig. 5b), leading to corresponding larger particle surface available for CNP growth.

In the series of counterflow flames F9-F12 the polydisperse model also captures the increase of volume fraction (Fig. 5c) and average primary particle diameters (Fig. 5d) with pressure. The simulated $f_v$ profiles well matches the experimental data at 2 atm, while as pressure rises from 3 to 5 atm model underestimation increases up to a factor of 1.5, which is still acceptable taking into account the estimated experimental uncertainty of ~30% in [42]. Fig. 5d shows that larger deviations between measured and simulated results are instead observed in the $D_{pp}$ profiles, despite the significant experimental uncertainty (up to 70%) associated with scattering and extinction measurements of carbonaceous particle morphology in counterflow diffusion flames [43]. Specifically, the measured peak $D_{pp}$ is characterized by a more pronounced increase from 2 to 5 atm, i.e., from 13 to 52 nm, respectively, compared to the model predictions, i.e., from 28 to 40 nm. The largest model deviations are observed at 5 atm, where the model underpredicts the measured peak $f_v$ and, in turn, $D_{pp}$. Moreover, the model predicts a steeper increase of the $D_{pp}$ profiles from ~0.45 cm from the fuel nozzle toward the particle stagnation plane ($z_{stg,p}$), where the larger primary particle diameters are reached. On the other hand, the model captures the increasing slope of the $D_{pp}$ profiles from 2 to 5 atm, due to a related increase of coalescence and growth processes [42], as well as the shift of the peak $D_{pp}$ location towards larger distances from the fuel nozzle as pressure increases (Fig. 5d).

Fig. 6 shows the contribution to the predicted $f_v$ and $D_{pp}$ profiles in Fig. 5 of the different classes of lumped pseudo species and physico-chemical processes considered in the proposed model, focusing on both the premixed flame F1 ($\phi$ = 2.34, left panels of Fig. 6) and the counterflow flame F9 (2 atm, right panels of Fig. 6). Fig. 6a-b show the temperature profile and the sooting zones in the two flames. As detailed in [38], the distinct flow profiles in laminar premixed and counterflow flames have a notable impact on the flame structure and the processes of

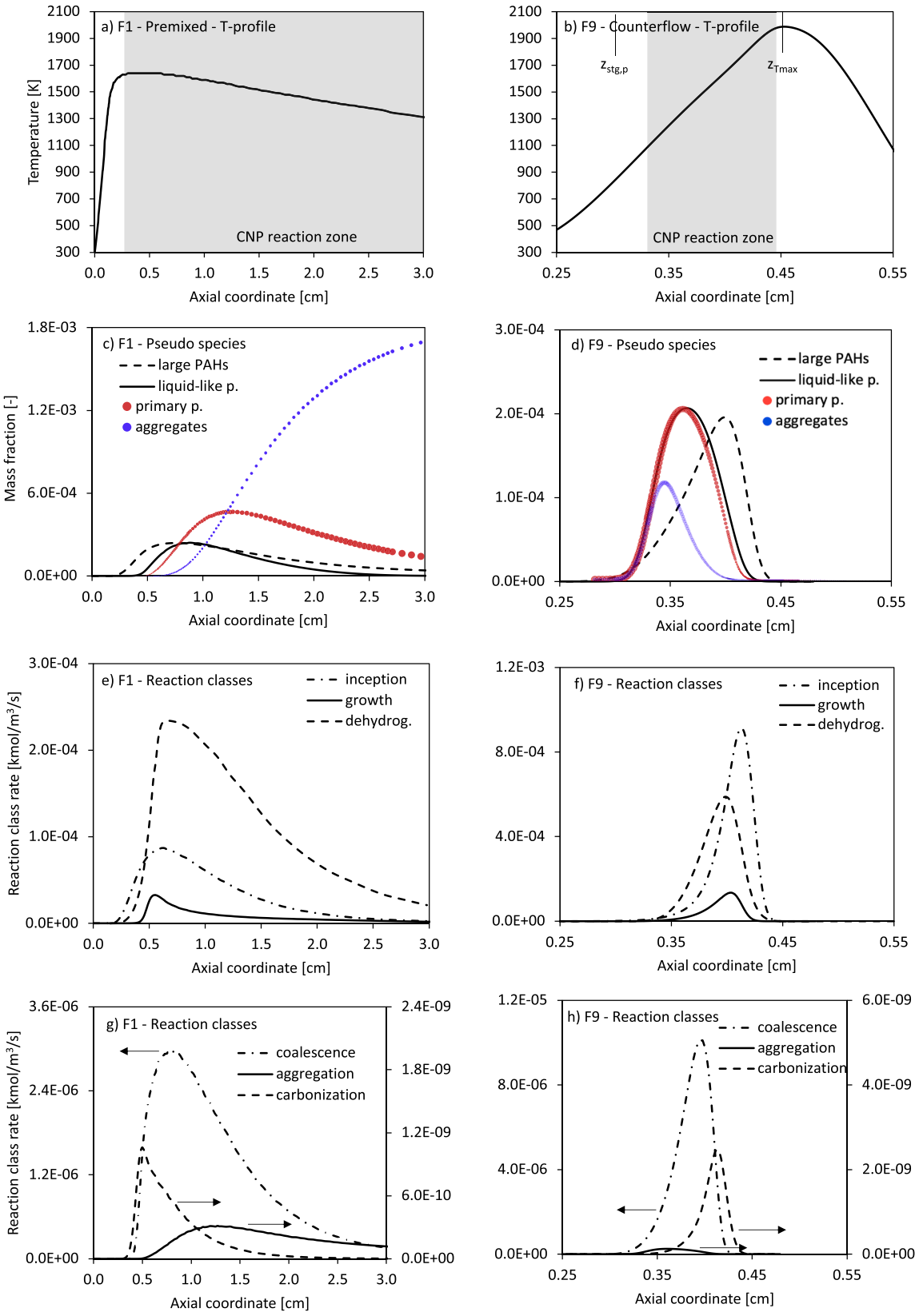


**Fig. 6.** Profiles of (a,b) temperature, c,d) mass fraction of the large PAH/CNP lumped pseudo species and e-h) reaction class rates for premixed-F1 (left panels) and counterflow-F9 (right panels) flames. In c) and d), larger circles indicate larger average primary particle diameters in the isolated primary particle (red) and aggregate (blue) profiles computed with the proposed model.

nucleation and growth. CNP formation in laminar premixed flames takes place as gaseous precursors are carried away from the burner head. Conversely, in the counterflow configuration, carbonaceous particles are generated near the rich side of the flame front, and the subsequent growth occurs in the region towards the particle stagnation plane, where CNPs are transported backward by thermophoresis.

In this regard, it is possible to observe in both F1 (Fig. 6c) and F9 (Fig. 6d) flames the transition from large PAHs (BIN1-4J in the proposed model) to liquid-like (BIN-L), solid primary particles (BIN-PP) and finally aggregates (BIN-AG), following the evolution of the pseudo-species considered in the polydisperse model and sketched in Fig. 1. In Fig. 6c-d the mass fraction profiles of isolated primary particles and aggregates are represented through a series of circles, whose size indicates the average primary particle diameter of BIN-PP and BIN-AG along the axial coordinate of the flame. Notably, while in the premixed flame the simulated mass fraction of aggregates overcomes that of primary particles at ~1.2 cm from the burner, in the counterflow flame isolated primary particles are more abundant than aggregates throughout the entire sooting region. Indeed, with respect to the premixed flame F1 (Fig. 6a), in the counterflow flame F9 larger temperatures are reached especially in the reaction region closer to the flame front $z_{Tmax}$ (Fig. 6b), fostering the growth and coalescence of primary particles towards larger isolated spherical entities rather than their aggregation towards fractal entities. In this regard, coalescence rates much larger than aggregation rates are obtained in the counterflow flame F9 (Fig. 6h) with respect to the premixed flame F1 (Fig. 6g).

The profiles of large PAHs (Fig. 6c-d) primarily follow those of the inception rates (Fig. 6e-f), which lead to liquid-like particles (BIN-L). Primary particles, instead, are firstly produced through carbonization of BIN-L (Fig. 6g-h), and then grow towards larger species or tend to aggregate, especially in the latest stage of CNP dynamics (for >1 cm from the burner in Fig. 6g and for <0.4 cm from the fuel nozzle in Fig. 6h). Coalescence of BIN-L with other liquid-like or solid particles (Fig. 6g-h) also contributes to the formation of larger carbonaceous species, with a rate lower than that of inception and surface growth but larger than carbonization and aggregation rates. In both flames, dehydrogenation reactions reduce the particle H/C ratio contributing to CNP graphitization in the entire sooting zone of both the F1 and F9 flames (Fig. 6e-f).

Finally, it is worth noting that the steep rise of the mass fraction profile of BIN-PP (red circles in Fig. 6d), becoming larger and larger due to both growth and coalescence, is responsible of the model overestimation of the average primary particle diameter in the early stage of CNP formation (dashed grey line in Fig. 5d). Conversely, the $D_{PP}$ profile in Fig. 5d slightly flattens from ~0.4 cm from the fuel nozzle up to the particle stagnation plane ($z_{stg,p}$), where aggregates made of primary particles with a similar size are produced (blue circles Fig. 6d).

A brute force sensitivity analysis on the investigated average primary particle profiles, carried out by modifying the reaction class rates governing CNP morphology, is discussed in Section 3.4.

### 3.2. Particle and primary particle size distributions

When modeling CNP polydispersity, it is important to study not only the profile of average diameters of primary particles, but also their distribution. In the experimental and numerical study on carbonaceous primary particles formed in ethylene coflow diffusion flame by Botero et al. [14], it was shown that not accurate predictions of primary particle size distributions (PPSD) can be obtained although the average primary particle diameters are satisfactorily modeled. Therefore, the PPSD measured by Amin et al. [43] through thermophoretic sampling of carbonaceous particles subsequently analyzed under transmission electron microscope (TEM) in a series of high-pressure counterflow diffusion ethylene flames (F17-F19 in Table 2) are here investigated. These measurements are, to the best of our knowledge, the only PPSD data proposed in the literature in laminar counterflow flames. However, it must be noted that only qualitative comparisons with model simulations can be performed, due to the large uncertainty of such experiments, in which the exact location of the collected carbonaceous particles is unknown and therefore it is not possible to investigate the spatial distribution of CNP properties [43]. PPSD obtained by image processing of > 400 primary particles sampled at each pressure [43] are qualitatively compared in Fig. 7, with numerical simulations in correspondence of the peak $f_v$ (solid lines) and 0.3 mm from the peak $f_v$ closer to the oxidizer nozzle (dashed lines). PPSD are calculated through the normalized results of Equation 2.

The evolution of PPSD was instead measured in an ethylene coflow diffusion flame [14], but its numerical simulation with the proposed model is hampered by the large number of lumped species and associated reactions considered. A proper model reduction, which is beyond the scope of this work, has to be performed in future studies to extend the model applicability to two-dimensional systems and to enable its validation against quantitative PPSD measurements.

Another morphological key property of carbonaceous nanoparticles is represented by the particle size distribution (PSD). Laminar premixed burner-stabilized stagnation (BSS) flame is the best configuration to experimentally study size distributions CNPs [31,75]. Here, the PSD measurements of Shao et al. [73], performed in a series of BSS ethylene flames (F6-F8 in Table 2) at different height above the burner and repeated in analogous conditions by different research groups [69,76], are selected to analyze the related model predictions (Fig. 8). For PSD simulations, the definition of particle diameter proposed by Camacho et al. [76] is used. Numerical results also account for the spatial shift due to probe effects, as suggested by Saggese et al. [77]. Fig. 8 also reports, for comparisons, simulations performed with the previous version of the present model [37], not accounting for CNP polydispersity, and with the detailed population balance model (PBM) recently proposed by Hou et al. [31].

The three models predict the increase of $f_v$ with the increase of the distance from the burner, i.e., with residence time, as shown in Fig. 8a. Specifically, the $f_v$ values computed with the model proposed in this works lay in between the results of its previous version and of the model proposed by Hou et al. [31] and have a maximum deviation from the measurements by a factor of 2.5 at $H_p = 10$ mm.

Larger differences between numerical results of the three models considered and the experimental data can be instead observed by analyzing PSD in Fig. 8b-d. The proposed model satisfactorily describes the transition from the unimodal to the bimodal distribution with the increase of particle residence time from $H_p = 5$ mm (Fig. 8b) to 10 mm (Fig. 8d). The onset of the PSD throat at $H_p = 7$ mm (Fig. 8c), indicating the segregation between the nucleation and coagulation mode experimentally observed [76], is instead obtained at a particle diameter (~3 nm) which is smaller than the measured one (~ 5 nm).

The clear development of the throat at $H_p = 10$ mm obtained with the proposed model represents another relevant improvement in the description of the PSD evolution with respect to its previous version [37], which considers neither CNP polydispersity nor the scaling of coalescence rates with the volume ratio of the colliding entities described in Section 2.1. However, there is still not clear experimental evidence about either a liquid-like behavior of the carbonaceous particles in the BSS flames investigated or the scaling adopted for coalescence rates. Future experimental measurements would enable a more extensive model validation and could help assessing the reliability of these assumptions in the proposed model.

Fig. 8c-d also show that the PBM model proposed by Hou et al. [31], which is not based on the discrete sectional approach but on the post-processing of a first simulation step through a stochastic method to resolve detailed particle morphology, features a very good agreement with the PSD data at $H_p = 5$ mm and the coagulation mode at larger distances from the burner, but it cannot properly capture the reduced but persistent nucleation mode at $H_p = 7$ and 10 mm. These results strengthen the predictive capability of the proposed model, also

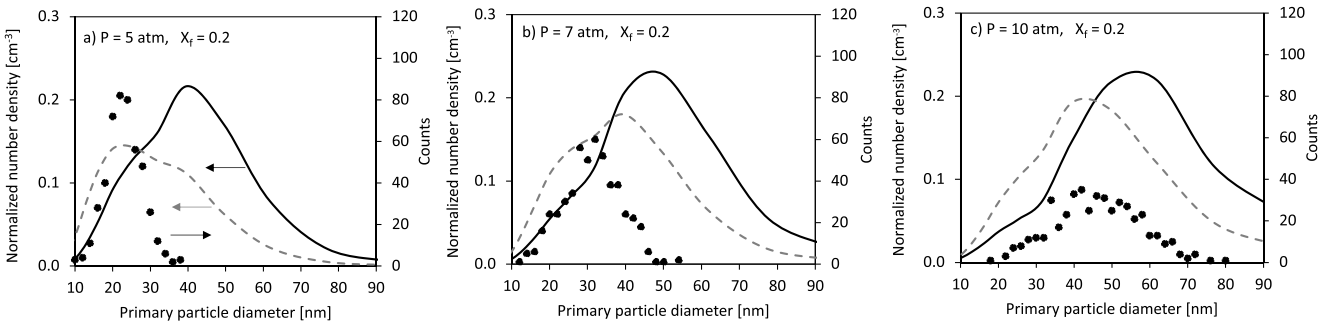


**Fig. 7.** Qualitative comparison of measured (symbols) and simulated (lines) primary particle size distribution in a) F17, b) F18, c) F19 counterflow ethylene flames (P = 5-10 atm, $X_f$=0.2, $K_G$=30 s$^{-1}$, $Z_{st}$=0.253 [43]). Simulated PPSD in correspondence of the peak $f_v$ (solid lines) and 0.3 mm closer to the oxidizer nozzle (dashed lines).

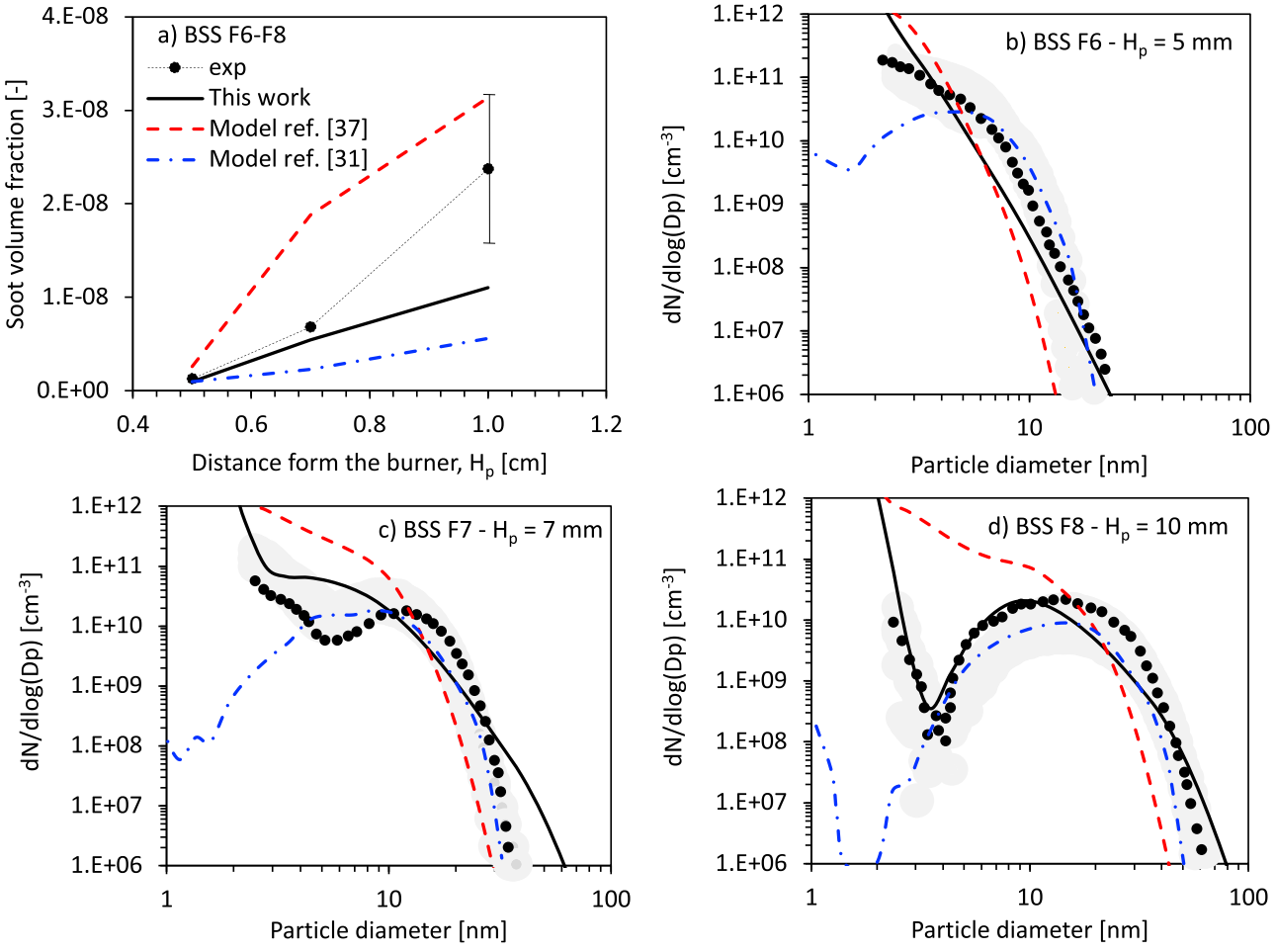


**Fig. 8.** a) $f_v$ and PSD at b) 5 mm, c) 7 mm and d) 10 mm from the burner in laminar ethylene premixed (P=1 atm, $v_0$=8 cm/s, $\phi$ =2.06, F9-F11 in Table 2) BSS flames. Symbols: experiments; lines: model simulations. Shaded area represents experimental uncertainty from measurements performed by different research groups in the same operating conditions [69,76]. Simulations with the PBM model are taken from Fig. 11 of [31,37].

highlighting the complexity in accurately describing PSD measurements of CNPs, which are characterized by large sensitivity to the different rate parameters of the CNP reaction classes, as discussed in [31] and in Section 3.4 of this work.

Similarly to Fig. 6, Fig. 9 shows the contribution of the different lumped pseudo-species to the simulated PSD at F6 ($H_p$ = 5 mm) and F8 ($H_p$ = 10 mm flames). In both flames, the nucleation mode is entirely constituted by liquid-like particles (BIN-L). Primary particles (BIN-PP), produced by carbonization process, are instead responsible of the coagulation mode obtained at $H_p$ = 10 mm for >10 nm species. At $H_p$ = 10 mm, aggregates of ~10-50 nm are also produced, but with a computed mass fraction which is lower (by a factor of ~2 for > 20 nm) than that of primary particles. In PSD measurements similar to those studied in Fig. 9, Wang et al. [78] observed only spherical particles up to 20 nm, while aggregates were detected for mobility sizes >30 nm in a laminar premixed BSS ethylene flame at $H_p$ = 1.2 mm. Deviations from sphericity of CNPs were also found in the experimental work by Camacho et al. [76] in BSS ethylene flames at both $H_p$ = 0.8 and 1.2 mm.

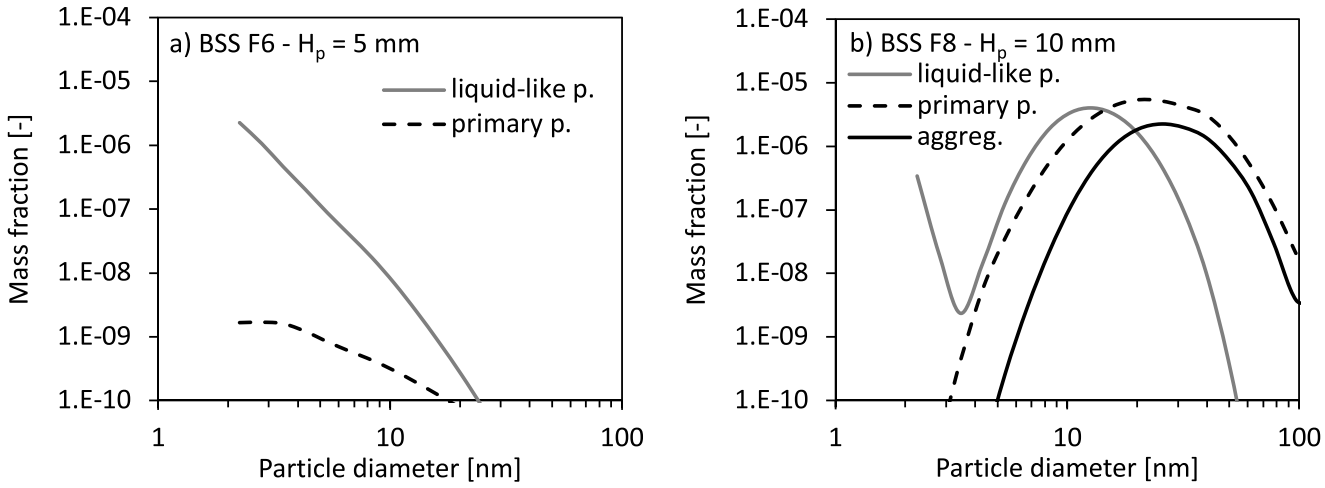


**Fig. 9.** Mass based contribution to the simulated PSD at a) $H_p = 5$ and b) $H_p = 10$ nm of the different carbonaceous lumped pseudo-species considered in the model.

Figs. 8 and 9 thus point at the key role played by carbonization mechanism and the updated coalescence rates considered in the proposed model for an improved description of PSD evolution with the increase of $H_p$ in BSS flames up to the pronounced bimodality observed at $H_p = 10$ mm.

### 3.3. Average particle size, number density and H/C ratio

Three additional properties of carbonaceous particles are analyzed, namely the average particle size, the number density and the H/C ratio of carbonaceous particles. The average particle size, expressed as the $D_{63}$ defined in [70], is modeled together with volume fraction profiles in a series of ethylene atmospheric counterflow flames at different strain

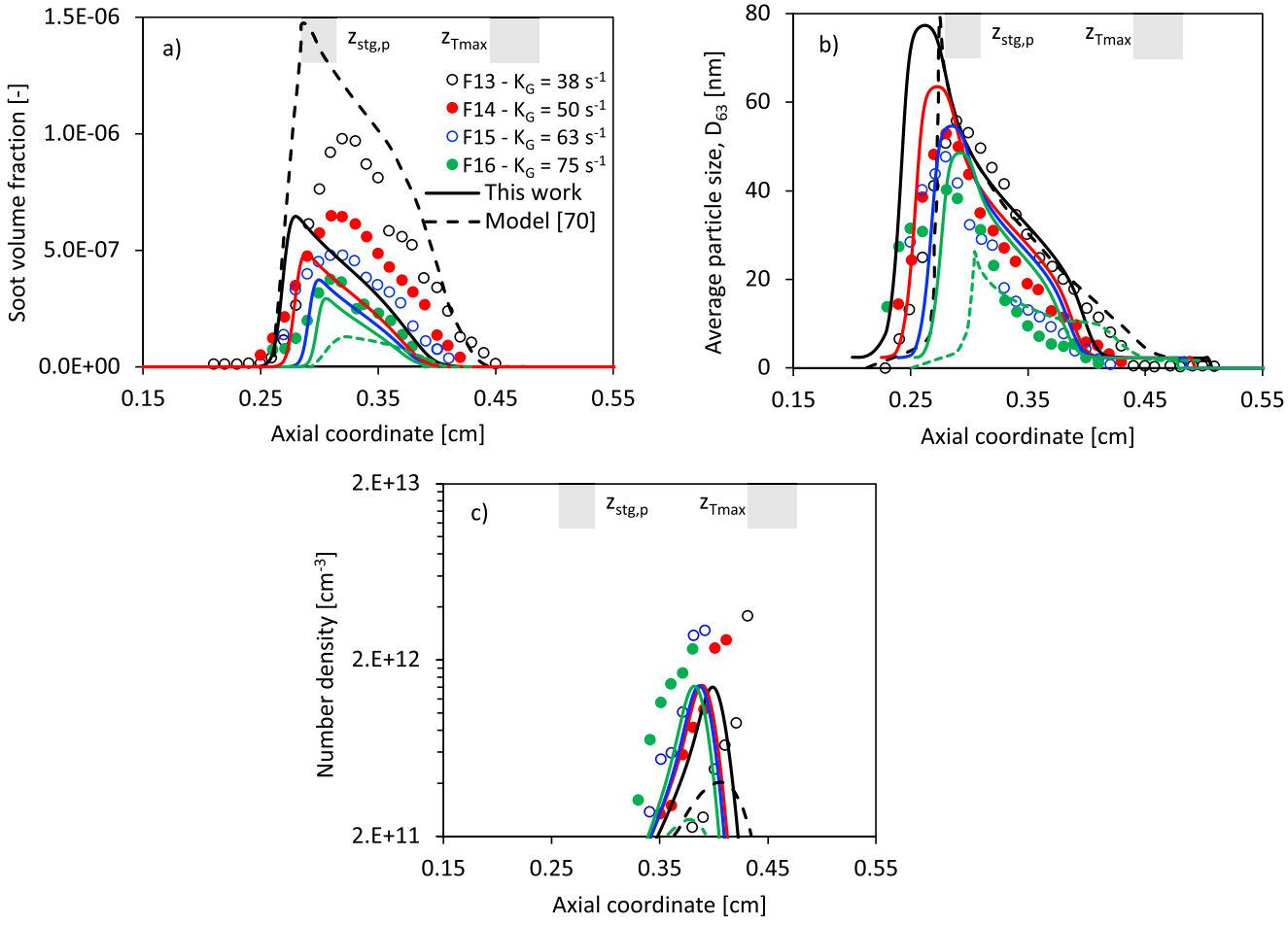


**Fig. 10.** a) $f_v$, b) CNP average particle size ($D_{63}$) and c) number density at different strain rates in laminar counterflow flames (F13: $K_G$=38 $s^{-1}$, F14: $K_G$=50 $s^{-1}$, F15: $K_G$=63 $s^{-1}$, F16: $K_G$=75 $s^{-1}$ in Table 2). Symbols: experiments [70]; lines: model simulations. Dashed lines are the results of the KAUST soot model [70] at $K_G$= 38 and 75 $s^{-1}$. Simulations with the KAUST model are taken from Figs. 9a and 10, 11 of [70].

rates (from $K_G = 38\ s^{-1}$ in F13 to $K_G = 75\ s^{-1}$ in F16) and compared with the related measurements [70] in Fig. 10.

Fig. 10a shows that both the measured and the simulated $f_v$ profiles increase with the decrease of strain rate, i.e., with the increase of residence time [63]. The polydisperse model also predicts the narrowing of the sooting zone as the strain rate increases, despite systematically underestimating the width of the $f_v$ profiles, especially at lower $K_G$ values. This model shortcoming is primarily due to uncertainties in the diffusivity of the BIN lumped species included in the model [45], and due to an increasing general underestimation with respect to volume fraction profile at lower strain rates (up to a factor of 1.6 for peak $f_v$ of flame F13). As regards the average particle size profiles in Fig. 10b, the model captures the decrease of $D_{63}$ with the increase of the global strain rate ($K_G$). In order to compare the polydisperse model with the performances of other literature kinetic mechanisms, Fig. 10 also shows the simulation results of flames F13 and F16 obtained with the KAUST model [35], based on the method of moments with interpolative closure [79] and accounting for inception, surface growth, and coalescence while neglecting particle aggregation [35,70].

CNP volume fraction is better predicted by the KAUST model at $K_G = 38\ s^{-1}$ with respect to the present model, while the opposite holds for flame F13 at $K_G = 75\ s^{-1}$ (Fig. 10a). Maximum deviations from the experiments are observed for flame F13 (Fig. 10b), where both models overestimate by a factor of 1.4 the measured peak $D_{63}$. Better quantitative agreement is also obtained with the proposed model against measured number density profiles in Fig. 10c, extending its satisfactorily predictive capability to other important morphological properties of CNPs.

Finally, model predictions of particle H/C ratio are validated against experimental data collected in two laminar premixed flames fueled by ethylene and methane by Russo et al. [40]. Condensed species and CNP concentration measurements, expressed in mg/Nl, are also provided in [40]. Model simulations well capture, qualitatively and quantitatively, the higher carbonaceous particle formation (Fig. 11a) in the ethylene flame, where more dehydrogenated particles (Fig. 11b) are produced with respect to methane flame due to the related lower fuel H/C ratio (2 for $C_2H_4$ and 4 for $CH_4$) [40]. These results highlight the good model description of carbonaceous nanostructure, which significantly determines not only the reactivity [10,80] but also the optical and electronic properties of CNPs, as discussed in the introduction of this work.

### 3.4. Brute force sensitivity analysis

When modeling CNP formation using discrete sections, BINs are pseudo species, and their reactions are therefore lumped. While elemental reactions have well-defined rate constants, lumped reactions can include more elemental steps, leading to less accurate rate constants and higher uncertainty [36]. Reaction rate uncertainties are even more amplified when dealing with the kinetics of physical carbonaceous particle processes such as particle carbonization, coalescence and aggregation, which are expressed in the Arrhenius form to be compliant with the CHEMKIN format [33]. The high sensitivity of the modeled CNP properties to some of these rate parameters was also analyzed in previous modeling studies based on methodologies other than the discrete sectional approach used for the present model [14,27,44].

Accordingly, a brute force sensitivity analysis is performed to assess the impact of the main pathways, and the related reaction class rates implemented in the proposed model, governing the evolution of the key morphological properties of carbonaceous particles in the several flames investigated.

Specifically, Fig. 12 shows the comparison between experiments and simulations performed with the proposed model and with three modified models for volume fraction ($f_v$) and average particle diameter ($D_{pp}$) profiles (Fig. 12a-f) in the premixed flame F3, $D_{pp}$ profile (Fig. 12c) in the counterflow flame F9, average particle size ($D_{63}$) profile (Fig. 12d) in the counterflow flame F13, and particle size distribution (PSD) in the BSS flames F6 and F8 at $H_p = 5$ and 10 mm, respectively (Fig. 12e-f). The modified models are here briefly described, with the related differences highlighted in Table 3:

- M1: with respect to base model (BM), a reference pre-exponential factor equal to $1.6 \times 10^{13}$ $cm^3/mol/s$ is assumed for coalescence and aggregation pathways, as in the previous version of model [37]. Conversely, in BM a reference pre-exponential factor larger by a factor of 2.5 is considered ($4.0 \times 10^{13}$ $cm^3/mol/s$ in Table 3).
- M2: with respect to BM, coalescence rates are calculated considering the temperature-, H/C ratio-, and size-dependent collision efficiency ($\gamma$) adopted for aggregation reactions based on the previous version of the model [37]. Moreover, consistently with [37], the coalescence rates in M2 are scaled based on the number of C-atoms ($nC^{1/6}$) of the colliding entities [37,54,62], rather than as a function of the volume ratio ($V_{big}/V_{small}$) of the colliding entities.
- M3: with respect to BM, the reference pre-exponential factor for carbonization reactions adopted from Dobbins [49] are maintained constant ($1.6 \times 10^{13}\ s^{-1}$), rather than scaled as a function of particle size and H/C ratio. Since the reference rate adopted represents an upper limit for carbonization kinetics, the modification in M3 leads to a much faster carbonization, especially for small liquid-like particles (BIN-L), with respect to BM (see Fig. S1 of the SM).

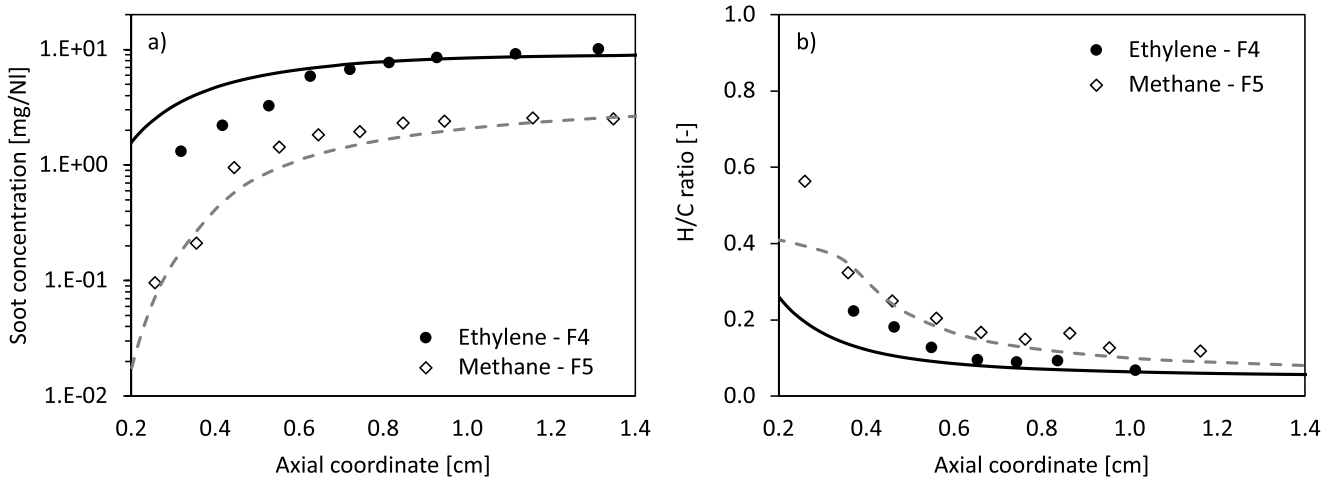


**Fig. 11.** a) CNP concentration and b) H/C ratio in laminar premixed ethylene (F4, P=1 atm, $v_0$=4 cm/s, $\phi$ =2.4) and methane (F5, P=1 atm, $v_0$=5 cm/s,$\phi$ =2.4) flames. Symbols: experiments [40]; lines: model simulations.

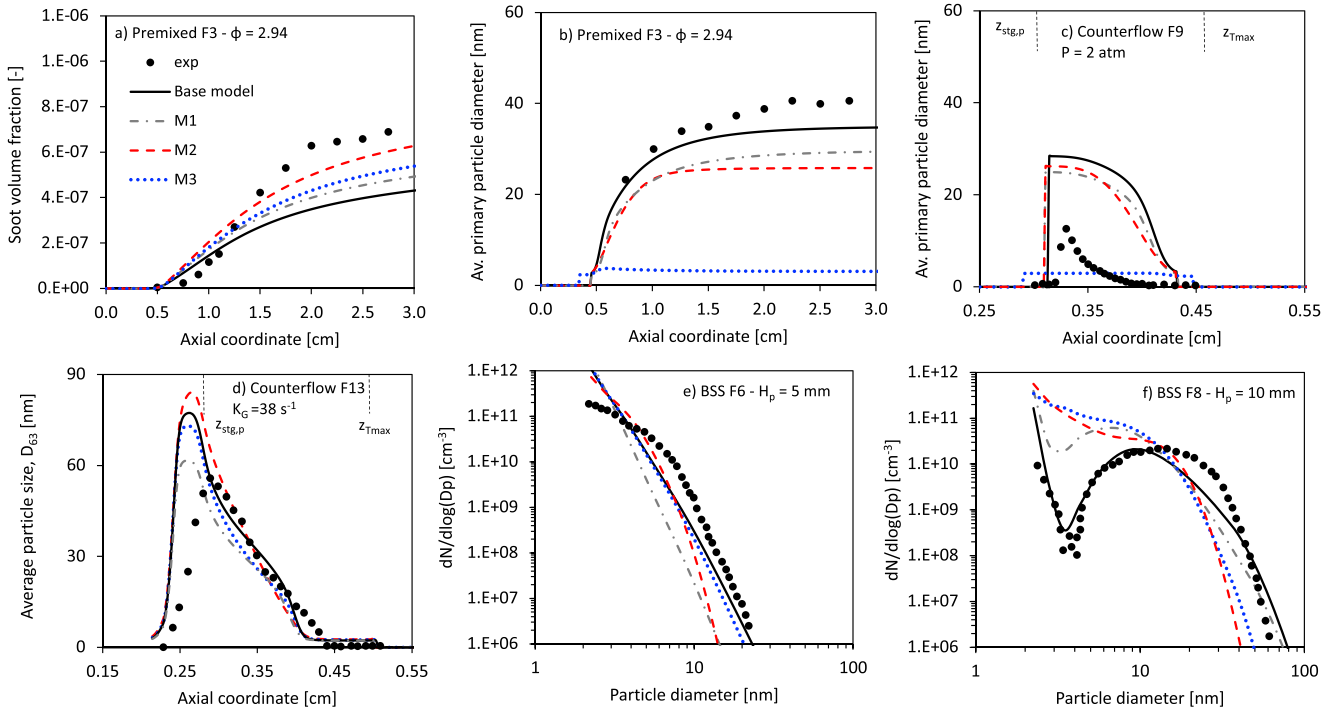


**Fig. 12.** Brute force sensitivity analysis results compared with the base model and the experimental data: a) $f_v$ profiles in F3; b) $D_{pp}$ profiles in F9; c) $D_{63}$ profiles in F13; e) PSD in F6; f) PSD in F8.

**Table 3**
Differences in the pre-exponential factors of the modified models used in the brute force sensitivity analysis.

| Model | Carbonization | Coalescence | Aggregation |
|---|---|---|---|
| Base model (BM) | $1.8\times10^{6}\frac{C/H}{C/H_{ref}}\frac{D}{D_{ref}}$ | $4.0\times10^{13}\frac{V_{big}}{V_{small}}$ | $4.0\times10^{13}\mathrm{nC}^{1/6}\gamma$ |
| M1 | not modified | $1.6\times10^{13}\frac{V_{big}}{V_{small}}$ | $1.6\times10^{13}\mathrm{nC}^{1/6}\gamma$ |
| M2 | not modified | $1.6\times10^{13}\mathrm{nC}^{1/6}\gamma$ | not modified |
| M3 | $1.8\times10^{6}$ | not modified | not modified |

The results of the brute force sensitivity analysis are listed below:

- M1: the albeit small reduction (by a factor of 2.5) of the reference coalescence pre-exponential factor leads to an evident worsening of model predictions for PSD at $H_p$=10 mm (Fig. 12f). In particular, the strong bimodality experimentally measured and predicted by BM becomes faint with M1 simulations. This result highlights the very high sensitivity of PSD to coalescence rates, especially at large distances from the burner, i.e., large particle residence times. Conversely, smaller deviations with respect to BM are observed for the other properties, with a slight reduction of $D_{pp}$ profile in both F3 and F9 flames (Fig. 12c-d) due to the reduced coalescence toward larger BIN-L, which are subsequently converted in BIN-PP though the carbonization process. Accordingly, a higher fraction of aggregates constituted by smaller primary particles, i.e., with a larger surface area, is produced in the premixed laminar flame F3, leading to a corresponding slightly higher $f_v$ profile with respect to BM in Fig. 12a.
- M2: in this case, deviations from BM are similar to those observed for M1 simulations. Without considering the scaling factor of coalescence rates based on the volume ratio of the colliding entities, it is impossible to describe the development of the PSD bimodality in BBS flame F8 (Fig. 12f). On the contrary, concerning $D_{63}$ profiles in Fig. 12d, M2 results show an opposite trend with respect to M1 when compared to BM simulations. In fact, the coalescence rates scaled as a function of the number of C-atoms of the colliding entities in M2 lead to a slower rise of $D_{63}$ profile in the first stage of carbonaceous particle growth closer to the flame front ($z_{Tmax}$ in Fig. 12d). Then, where larger carbonaceous species are formed towards the particle stagnation plane ($z_{stg,p}$), coalescence rates become faster than those in BM, leading to a corresponding higher peak $D_{63}$ (Fig. 12d).
- M3: by considering the reference carbonization rates proposed by Dobbins [49] as constant, i.e., independent of particle size and H/C ratio, small liquid-like particles are much more rapidly converted to primary particles, as discussed above, leading to extremely small average primary particle diameters in both the premixed flame F3 (Fig. 12b) and the counterflow flame F9 (Fig. 12c). The much smaller $D_{pp}$ in Fig 12b implies larger particle surface available for growth reactions, thus larger $f_v$ closer to the experiments with respect to the base model (Fig. 12a), which however captures the trend of $f_v$ with the equivalence ratio (Fig. 5a) and which conversely shows a better agreement against $f_v$ measurements for $\phi = 2.34$ in flame F1 compared to models M1-M3 (see Fig. S3 of the SM). Also, without scaling carbonization rates, it is not possible to predict the bimodal PSD in Fig. 12f. In fact, the fast carbonization kinetics in M3 leads to the predominance of solid primary particles rather than liquid-like species at a large distance from the burner ($H_p$ = 10 mm) in the BSS flame F8, and the evolution of PSD is controlled by aggregation rather than by coalescence. Since aggregation is not scaled as a function of the volume ratio of the colliding entities, the pronounced throat in the PSD in Fig. 12f cannot be reproduced.

It is remarked that the brute force sensitivity analysis performed is focused on the reaction classes introduced or modified in the proposed model from its previous versions [36,37] and that primarily control the evolution of carbonaceous particle morphology. Therefore, this analysis does not entirely cover the kinetics of all the pathways considered in the proposed model, which are also characterized by uncertainties and underlying assumptions since addressed to lumped pseudo species and non-elementary chemical steps. Nevertheless, the results of Fig. 12 point not only at the high sensitivity of CNP morphology to the reaction class

rates adopted for carbonization, coalescence and aggregation, but, more in general, they underline the complexity of tracking with a single kinetic model the several key properties of carbonaceous particles produced by the high-temperature combustion of hydrocarbons. As suggested in [14], the lack of understanding of individual sooting processes at current stage could be partially filled with future dedicated molecular dynamics studies and wider experimental campaigns.

## 4. Conclusions

A novel detailed discrete sectional model for CNP formation has been presented in this work. The main novelty introduced is the description of CNP polydispersity achieved by considering the formation of primary particles with different sizes from liquid-like counterparts through the carbonization process. This process involves the physical rearrangement of the internal structure of carbonaceous particles. Compared to previous versions of the model, this allows to predict the evolution of average primary particle diameters ($D_{pp}$) measured in both premixed and counterflow diffusion ethylene flames, varying the equivalence ratio and the pressure, respectively. The evolution of primary particle size distributions from 5 to 10 atm in a series of counterflow ethylene flames is also qualitatively described. The model captures the measured trends of volume fraction (with maximum deviations within a factor of 2.5 from the experiments), average particle size ($D_{63}$), particle size distribution (PSD), number density, as well as the particle H/C ratio profiles measured in two premixed flames fueled by ethylene and methane, respectively. In the series of laminar counterflow ethylene flames varying pressure from 2 to 5 atm, however, simulated $D_{pp}$ profiles feature a steeper rise from the flame front towards the particle stagnation plane compared to the experiments. This is primarily due to a too fast coalescence between the liquid-like and the solid CNP pseudo-species (BINs) considered.

On the other hand, beyond the significant improved description of CNP morphology compared with its previous versions, it has been shown that the current model performances are competitive with other state of the art models developed based on different approaches, such as the method of moments or the stochastic approach. It has to be underlined that this model is at the beginning of its possible evolution. A lot of work has to be done to arrive at satisfactory agreements with the experimental data. Future studies are thus necessary to perform more accurate rate estimation of key processes like carbonization, coalescence and aggregation, characterized by the largest uncertainties. All these reactions significantly affect model predictions of CNP morphology, as shown through a brute force sensitivity analysis. Anyway, we strongly believe that sharing this model with the scientific community can be a starting point in the process of better understanding the characteristics of non-functionalized CNPs and, possibly, similar carbon-based nanomaterials with surface functionalization, and that several research groups can contribute to this needed effort.

A final observation is that the proposed model comprises a critical number of species and reactions, which prevents its use in multi-dimensional reactors and flames simulations. Future studies are necessary to identify solutions for an effective reduction of this kinetic mechanism, without losing the capability of characterizing the morphology and the nanostructure of the CNPs.

## CRediT authorship contribution statement

**Andrea Nobili:** Writing – original draft, Methodology, Conceptualization. **Niccolò Fanari:** Validation, Investigation. **Timoteo Dinelli:** Software, Formal analysis. **Edoardo Cipriano:** Software. **Alberto Cuoci:** Software, Methodology. **Matteo Pelucchi:** Writing – review & editing, Funding acquisition. **Alessio Frassoldati:** Methodology, Investigation, Conceptualization. **Tiziano Faravelli:** Writing – review & editing, Supervision, Conceptualization.

## Declaration of competing interest

The authors declare that they have no known competing financial interests or personal relationships that could have appeared to influence the work reported in this paper.

## Acknowledgments

This research was financially supported by the PRIN PNRR P2022P7XHA “Hydrogen and carbon black production from cracking in molten media” (HAMMER).

## Supplementary materials

Supplementary material associated with this article can be found, in the online version, at doi:10.1016/j.combustflame.2024.113697.

## References

[1] R.P. Lindstedt, H.A. Michelsen, M.E. Mueller, Special issue and perspective on the chemistry and physics of carbonaceous particle formation, Combust. Flame (2023) 113042.
[2] S. Singh, P.K. Bairagi, N. Verma, Candle soot-derived carbon nanoparticles: an inexpensive and efficient electrode for microbial fuel cells, Electrochim. Acta 264 (2018) 119–127.
[3] C. Liu, A.V. Singh, C. Saggese, Q. Tang, D. Chen, K. Wan, M. Vinciguerra, M. Commodo, G. De Falco, P. Minutolo, A. D'Anna, H. Wang, Flame-formed carbon nanoparticles exhibit quantum dot behaviors, Proc. Natl. Acad. Sci. U. S. A. 116 (2019) 12692–12697.
[4] G. De Falco, G. Mattiello, M. Commodo, P. Minutolo, X. Shi, A. D'Anna, H. Wang, Electronic band gap of flame-formed carbon nanoparticles by scanning tunneling spectroscopy, Proc. Combust. Inst. 38 (2021) 1805–1812.
[5] P. Minutolo, M. Commodo, A. D'Anna, Optical properties of incipient soot, Proc. Combust. Inst. 39 (2023) 1129–1138.
[6] K. Wan, X. Shi, H. Wang, Quantum confinement and size resolved modeling of electronic and optical properties of small soot particles, Proc. Combust. Inst. 38 (2021) 1517–1524.
[7] C. Russo, B. Apicella, A. Ciajolo, Blue and green luminescent carbon nanodots from controllable fuel-rich flame reactors, Sci. Rep. 9 (2019) 14566.
[8] M. Sirignano, C. Russo, A. Ciajolo, One-step synthesis of carbon nanoparticles and yellow to blue fluorescent nanocarbons in flame reactors, Carbon 156 (2020) 370–377. N. Y.
[9] S. Bocchicchio, M. Commodo, L.A. Sgro, M. Chiari, A. D'Anna, P. Minutolo, Thermo-optical-transmission OC/EC and Raman spectroscopy analyses of flame-generated carbonaceous nanoparticles, Fuel 310 (2022) 122308.
[10] M. Alfè, B. Apicella, R. Barbella, J.N. Rouzaud, A. Tregrossi, A. Ciajolo, Structure–property relationship in nanostructures of young and mature soot in premixed flames, Proc. Combust. Inst. 32 (2009) 697–704.
[11] M.N. Ess, D. Ferry, E.D. Kireeva, R. Niessner, F.X. Ouf, N.P. Ivleva, In situ Raman microspectroscopic analysis of soot samples with different organic carbon content: Structural changes during heating, Carbon 105 (2016) 572–585. N. Y.
[12] G.A. Kelesidis, E. Goudeli, S.E. Pratsinis, Morphology and mobility diameter of carbonaceous aerosols during agglomeration and surface growth, Carbon 121 (2017) 527–535. N. Y.
[13] J. Rissler, M.E. Messing, A.I. Malik, P.T. Nilsson, E.Z. Nordin, M. Bohgard, M. Sanati, J.H. Pagels, Effective density characterization of soot agglomerates from various sources and comparison to aggregation theory, Aerosol Sci. Technol. 47 (2013) 792–805.
[14] M.L. Botero, N. Eaves, J.A.H. Dreyer, Y. Sheng, J. Akroyd, W. Yang, M. Kraft, Experimental and numerical study of the evolution of soot primary particles in a diffusion flame, Proc. Combust. Inst. 37 (2019) 2047–2055.
[15] N. Morgan, M. Kraft, M. Balthasar, D. Wong, M. Frenklach, P. Mitchell, Numerical simulations of soot aggregation in premixed laminar flames, in: Proceedings of the Combustion Institute. 31 I, 2007.
[16] Q. Zhang, H. Guo, F. Liu, G.J. Smallwood, M.J. Thomson, Modeling of soot aggregate formation and size distribution in a laminar ethylene/air coflow diffusion flame with detailed PAH chemistry and an advanced sectional aerosol dynamics model, Proc. Combust. Inst. 32 (2009) 761–768.
[17] M. Balthasar, M. Frenklach, Detailed kinetic modeling of soot aggregate formation in laminar premixed flames, Combust. Flame 140 (2005) 130–145.
[18] S.B. Dworkin, Q. Zhang, M.J. Thomson, N.A. Slavinskaya, U. Riedel, Application of an enhanced PAH growth model to soot formation in a laminar coflow ethylene/air diffusion flame, Combust. Flame 158 (2011) 1682–1695.
[19] Q. Zhang, M.J. Thomson, H. Guo, F. Liu, G.J. Smallwood, A numerical study of soot aggregate formation in a laminar coflow diffusion flame, Combust. Flame 156 (2009) 697–705.
[20] S.H. Park, S.N. Rogak, W.K. Bushe, J.Z. Wen, M.J. Thomson, An aerosol model to predict size and structure of soot particles, Combust. Theory Model. 9 (2005) 499–513.

[21] M.R. Kholghy, N.A. Eaves, A. Veshkini, M.J. Thomson, The role of reactive PAH dimerization in reducing soot nucleation reversibility, Proc. Combust. Inst. 37 (2019) 1003–1011.
[22] N.A. Eaves, S.B. Dworkin, M.J. Thomson, Assessing relative contributions of PAHs to soot mass by reversible heterogeneous nucleation and condensation, Proc. Combust. Inst. 36 (2017) 935–945.
[23] A.L. Bodor, B. Franzelli, T. Faravelli, A. Cuoci, A post processing technique to predict primary particle size of sooting flames based on a chemical discrete sectional model: application to diluted coflow flames, Combust. Flame 208 (2019) 122–138.
[24] M. Sander, R.H. West, M.S. Celnik, M. Kraft, A Detailed model for the sintering of polydispersed nanoparticle agglomerates, Aerosol Sci. Technol. 43 (2009) 978–989.
[25] M.S. Celnik, M. Sander, A. Raj, R.H. West, M. Kraft, Modelling soot formation in a premixed flame using an aromatic-site soot model and an improved oxidation rate, Proc. Combust. Inst. 32 (2009) 639–646.
[26] A. Raj, M. Celnik, R. Shirley, M. Sander, R. Patterson, R. West, M. Kraft, A statistical approach to develop a detailed soot growth model using PAH characteristics, Combust. Flame 156 (2009) 896–913.
[27] D. Hou, C.S. Lindberg, M.Y. Manuputty, X. You, M. Kraft, Modelling soot formation in a benchmark ethylene stagnation flame with a new detailed population balance model, Combust. Flame 203 (2019) 56–71.
[28] C.S. Lindberg, M.Y. Manuputty, E.K.Y. Yapp, J. Akroyd, R. Xu, M. Kraft, A detailed particle model for polydisperse aggregate particles, J. Comput. Phys. 397 (2019) 108799.
[29] N.A. Fuchs, R.E. Daisley, M. Fuchs, C.N. Davies, M.E. Straumanis, The mechanics of aerosols, Phys. Today 18 (1965) 73.
[30] G.A. Kelesidis, E. Goudeli, S.E. Pratsinis, Flame synthesis of functional nanostructured materials and devices: surface growth and aggregation, Proc. Combust. Inst. 36 (2017) 29–50.
[31] D. Hou, C.S. Lindberg, M. Wang, M.Y. Manuputty, X. You, M. Kraft, Simulation of primary particle size distributions in a premixed ethylene stagnation flame, Combust. Flame 216 (2020) 126–135.
[32] M.R. Kholghy, G.A. Kelesidis, Surface growth, coagulation and oxidation of soot by a monodisperse population balance model, Combust. Flame 227 (2021) 456–463.
[33] R.J. Kee, F.M. Rupley, E. Meeks, J.A. Miller, CHEMKIN-III: a fortran chemical kinetics package for the analysis of gas phase chemical and plasma kinetics," Sandia National Laboratories Report, (1996).
[34] I.M. Kennedy, Models of soot formation and oxidation, Prog. Energy Combust. Sci. 23 (1997) 95–132.
[35] Y. Wang, A. Raj, S.H. Chung, Soot modeling of counterflow diffusion flames of ethylene-based binary mixture fuels, Combust. Flame 162 (2015) 586–596.
[36] C. Saggese, S. Ferrario, J. Camacho, A. Cuoci, A. Frassoldati, E. Ranzi, H. Wang, T. Faravelli, Kinetic modeling of particle size distribution of soot in a premixed burner-stabilized stagnation ethylene flame, Combust. Flame 162 (2015) 3356–3369.
[37] W. Pejpichestakul, A. Frassoldati, A. Parente, T. Faravelli, Kinetic modeling of soot formation in premixed burner-stabilized stagnation ethylene flames at heavily sooting condition, Fuel 234 (2018) 199–206.
[38] A. Nobili, A. Cuoci, W. Pejpichestakul, M. Pelucchi, C. Cavallotti, T. Faravelli, Modeling soot particles as stable radicals: a chemical kinetic study on formation and oxidation. Part I. Soot formation in ethylene laminar premixed and counterflow diffusion flames, Combust. Flame 243 (2022) 112073.
[39] A. Nobili, W. Pejpichestakul, M. Pelucchi, A. Cuoci, C. Cavallotti, T. Faravelli, Modeling soot particles as stable radicals: a chemical kinetic study on formation and oxidation. Part II. Soot oxidation in flow reactors and laminar flames, Combust. Flame 243 (2022) 112072.
[40] C. Russo, A. Tregrossi, A. Ciajolo, Dehydrogenation and growth of soot in premixed flames, Proc. Combust. Inst. 35 (2015) 1803–1809.
[41] A. Nobili, L. Pratali Maffei, A. Baggioli, M. Pelucchi, A. Cuoci, C. Cavallotti, T. Faravelli, On the radical behavior of large polycyclic aromatic hydrocarbons in soot formation and oxidation, Combust. Flame (2021) 111692.
[42] H.M.F. Amin, W.L. Roberts, Soot measurements by two angle scattering and extinction in an N2-diluted ethylene/air counterflow diffusion flame from 2 to 5 atm, Proc. Combust. Inst. 36 (2017) 861–869.
[43] H.M.F. Amin, A. Bennett, W.L. Roberts, Determining fractal properties of soot aggregates and primary particle size distribution in counterflow flames up to 10 atm, Proc. Combust. Inst. 37 (2019) 1161–1168.
[44] M.R. Kholghy, A. Veshkini, M.J. Thomson, The core–shell internal nanostructure of soot – A criterion to model soot maturity, Carbon 100 (2016) 508–536. N. Y.
[45] A.D. Abid, E.D. Tolmachoff, D.J. Phares, H. Wang, Y. Liu, A. Laskin, Size distribution and morphology of nascent soot in premixed ethylene flames with and without benzene doping, Proc. Combust. Inst. 32 (2009) 681–688.
[46] R.L. Vander Wal, Soot precursor carbonization: Visualization using LIF and LII and comparison using bright and dark field TEM, Combust. Flame 112 (1998) 607–616.
[47] H.A. Michelsen, M.B. Colket, P.E. Bengtsson, A. D'Anna, P. Desgroux, B.S. Haynes, J.H. Miller, G.J. Nathan, H. Pitsch, H. Wang, A review of terminology used to describe soot formation and evolution under combustion and pyrolytic conditions, ACS Nano 14 (2020) 12470–12490.
[48] C. Russo, M. Alfè, J.N. Rouzaud, F. Stanzione, A. Tregrossi, A. Ciajolo, Probing structures of soot formed in premixed flames of methane, ethylene and benzene, Proc. Combust. Inst. 34 (2013) 1885–1892.
[49] R.A. Dobbins, Soot inception temperature and the carbonization rate of precursor particles, Combust. Flame 130 (2002) 204–214.
[50] R.H. Hurt, G.P. Crawford, H.S. Shim, Equilibrium nanostructure of primary soot particles, Proc. Combust. Inst. 28 (2000) 2539–2546.
[51] Q. Zhang, H. Guo, F. Liu, G.J. Smallwood, M.J. Thomson, Implementation of an advanced fixed sectional aerosol dynamics model with soot aggregate formation in a laminar methane/air coflow diffusion flame, Combust. Theory Model. 12 (2008) 621–641.
[52] M. Schenk, S. Lieb, H. Vieker, A. Beyer, A. Gölzhäuser, H. Wang, K. Kohse-Höinghaus, Morphology of nascent soot in ethylene flames, Proc. Combust. Inst. 35 (2015) 1879–1886.
[53] H. Richter, S. Granata, W.H. Green, J.B. Howard, Detailed modeling of PAH and soot formation in a laminar premixed benzene/oxygen/argon low-pressure flame, Proc. Combust. Inst. 30 (2005) 1397–1405.
[54] M. Sirignano, A. D'Anna, Coagulation of combustion generated nanoparticles in low and intermediate temperature regimes: An experimental study, Proc. Combust. Inst. 34 (2013) 1877–1884.
[55] L. Henderson, P. Shukla, V. Rudolph, S.K. Bhatia, Modelling the formation, growth and coagulation of soot in a combustion system using a 2-D population balance model, Combust. Flame 245 (2022) 112303.
[56] Y.R. Zhang, K.H. Luo, Regimes of head-on collisions of equal-sized binary droplets, Langmuir 35 (2019) 8896–8902.
[57] G.A. BACH, D.L. KOCH, A. GOPINATH, Coalescence and bouncing of small aerosol droplets, J. Fluid Mech. 518 (2004) 157–185.
[58] B. Wang, S. Mosbach, S. Schmutzhard, S. Shuai, Y. Huang, M. Kraft, Modelling soot formation from wall films in a gasoline direct injection engine using a detailed population balance model, Appl. Energy 163 (2016) 154–166.
[59] T.A. Sipkens, A. Boies, J.C. Corbin, R.K. Chakrabarty, J. Olfert, S.N. Rogak, Overview of methods to characterize the mass, size, and morphology of soot, J. Aerosol. Sci. 173 (2023) 106211.
[60] A.W. Adamson, A.P. Gast, Physical Chemistry of Surfaces, Interscience publishers, New York, 1967.
[61] T. Hawa, M.R. Zachariah, Coalescence kinetics of unequal sized nanoparticles, J. Aerosol. Sci. 37 (2006) 1–15.
[62] A. D'Anna, M. Sirignano, J. Kent, A model of particle nucleation in premixed ethylene flames, Combust. Flame 157 (2010) 2106–2115.
[63] W. Koch, S.K. Friedlander, The effect of particle coalescence on the surface area of a coagulating aerosol, J. Colloid. Interface Sci. 140 (1990) 419–427.
[64] M.v. Smoluchowski, Grundriß der Koagulationskinetik kolloider Lösungen, Kolloid-Z. 21 (1917) 98–104.
[65] E. Ranzi, A. Frassoldati, R. Grana, A. Cuoci, T. Faravelli, A.P. Kelley, C.K. Law, Hierarchical and comparative kinetic modeling of laminar flame speeds of hydrocarbon and oxygenated fuels, Prog. Energy Combust. Sci. 38 (2012) 468–501.
[66] L. Pratali Maffei, M. Pelucchi, T. Faravelli, C. Cavallotti, Theoretical kinetics of HO2 + C5H5: a missing piece in cyclopentadienyl radical oxidation reactions, Proc. Combust. Inst. 39 (2023) 695–703.
[67] A. Cuoci, A. Frassoldati, T. Faravelli, E. Ranzi, OpenSMOKE++: an object-oriented framework for the numerical modeling of reactive systems with detailed kinetic mechanisms, Comput. Phys. Commun. 192 (2015) 237–264.
[68] D. Zheng, A. Nobili, A. Cuoci, M. Pelucchi, X. Hui, T. Faravelli, Soot formation from n-heptane counterflow diffusion flames: Two-dimensional and oxygen effects, Combust. Flame (2022) 112441.
[69] International Sooting Flame (ISF) Workshop: www.adelaide.edu.au/cet/isfworkshop. 2024.
[70] Y. Wang, S.H. Chung, Strain rate effect on sooting characteristics in laminar counterflow diffusion flames, Combust. Flame 165 (2016) 433–444.
[71] E. Ramalli, T. Dinelli, A. Nobili, A. Stagni, B. Pernici, T. Faravelli, Automatic validation and analysis of predictive models by means of big data and data science, Chem. Eng. J. 454 (2023) 140149.
[72] F. Xu, P.B. Sunderland, G.M. Faeth, Soot formation in laminar premixed ethylene/air flames at atmospheric pressure, Combust. Flame 108 (1997) 471–493.
[73] C. Shao, F. Campuzano, Y. Zhai, H. Wang, W. Zhang, S. Mani Sarathy, Effects of ammonia addition on soot formation in ethylene laminar premixed flames, Combust. Flame 235 (2022) 111698.
[74] Y. Wang, S.H. Chung, Soot formation in laminar counterflow flames, Prog. Energy Combust. Sci. 74 (2019) 152–238.
[75] A.D. Abid, J. Camacho, D.A. Sheen, H. Wang, Quantitative measurement of soot particle size distribution in premixed flames – The burner-stabilized stagnation flame approach, Combust. Flame 156 (2009) 1862–1870.
[76] J. Camacho, C. Liu, C. Gu, H. Lin, Z. Huang, Q. Tang, X. You, C. Saggese, Y. Li, H. Jung, L. Deng, I. Wlokas, H. Wang, Mobility size and mass of nascent soot particles in a benchmark premixed ethylene flame, Combust. Flame 162 (2015) 3810–3822.
[77] C. Saggese, A. Cuoci, A. Frassoldati, S. Ferrario, J. Camacho, H. Wang, T. Faravelli, Probe effects in soot sampling from a burner-stabilized stagnation flame, Combust. Flame 167 (2016) 184–197.
[78] M. Wang, Q. Tang, J. Mei, X. You, On the effective density of soot particles in premixed ethylene flames, Combust. Flame 198 (2018) 428–435.
[79] M. Frenklach, Method of moments with interpolative closure, Chem. Eng. Sci. 57 (2002) 2229–2239.
[80] R.L. Vander Wal, A.J. Tomasek, Soot nanostructure: dependence upon synthesis conditions, Combust. Flame 136 (2004) 129–140.